Study of potential formation and low frequency fluctuations in the GAMMA10 tandem mirror

Masanori Mizuguchi

February 2014

Study of potential formation and low frequency fluctuations in the GAMMA10 tandem mirror

Masanori Mizuguchi

Doctoral Program in Physics

Submitted to the Graduate School of

Pure and Applied Sciences

in Partial Fulfillment of the Requirements

for the Degree of Doctor of Philosophy in

Science

at the

University of Tsukuba

Contents

1. Introduction

One of the most important issues in the magnetic confinement plasma is to study the mechanism of anomalous transport. There are classical and neoclassical theories for plasma transport. However, the particle and energy transports observed experimentally in most devices are much larger than those expected in the classical and neoclassical theories. These transports are called anomalous transport. It is considered that the anomalous transport is caused by turbulence of various instabilities. In the improved confinement mode called H-mode, reduction of particle and energy transports, decrease of turbulence level, radial electric field and E×B drift shear caused by electric field were observed. Relation between electric field and turbulence fluctuation has been studied [1-16]. There are the attempts to control the potential or electric field with active control methods to study the relation between the electric field and the fluctuation. There is the plasma heating as an example of the potential control methods. The relation between radial particle flux and electric field for the ECH plasma on TJ-II is shown in Fig. 1.1 [13]. The particle flux excited in the case of almost no electric field is gradually suppressed with an increase or decrease in electric field. In this study, the electric field was controlled by electron cyclotron heating systems. The other potential control methods (e.g. electric biasing) were also employed in various devices [17-24]. Figure 1.2 – 1.4 shows schematic view of the setup and result in the biased experiment on Q_T-Upgrade machine [24]. The radial potential profile is changed by electric biasing, and then, the instability appears to be suppressed with an increase or decrease in bias voltage. The changing boundary condition method is useful to study the relation between the electric field and the fluctuation.

The relation between the electric field and the fluctuation was also studied in GAMMA10. Figure 1.5 shows radial profile of the potential fluctuation level of the drift-type fluctuation as a function of RF power [15]. The electron diamagnetic drift frequency and E×B drift frequency are estimated as shown in Fig. 1.6 (a) and (b). Then, the difference between the drift type frequency and observed frequency has a correlation with the value of $\sin(\alpha_{n\varphi})$ as shown in Fig. 1.6 (c). In addition, it was indicated that the dependence of the density fluctuation level which is driven E×B drift on phase difference $\sin(\alpha_{n\varphi})$ varies with radial position [16]. Suppression of the drift-type fluctuation due to applying electron cyclotron heating (ECH) at the plug region has been observed in GAMMA 10 [11]. When the plug ECH is applied, central plasma potential increases at R ~ 0 cm. The potential control experiments with end plate biasing were also carried out in GAMMA10 [21,22]. The radial electric field E_r was controlled by varying a bias voltage applied on the radially segmented end plates. Figure 1.7 shows the location of the end plates and the magnetic field lines on GAMMA10. Figure 1.8 shows radial profiles of the fluctuation level, the central potential and the electric field for bias voltage V_B = 1 kV during the formation of confining potentials by applying the plug ECH. They are suppressed by applying moderate negative bias to lower the radial electric field. It may be possible to control the plasma instabilities by shaping the radial potential profiles. There is the other attempt to the potential or electric field control on GAMMA10 [23,25,26]. Figure 1.9 shows the central potential, the fluctuation frequency, and the fluctuation amplitude against end plate resistance. When the resistance is smaller, the radial electric field is estimated as higher since the potential higher with no change of floating potential of the segmented limiter. The increase of the electric field and the upshift of the frequency suggest the E×B rotation is the main drive of the fluctuation. The similar dependences of the phase difference between the density fluctuation and the electric field are observed in the core region, although, the linear dependence on the density fluctuation is observed in the peripheral region and the dependence becomes weaker

with the increase of the electric field. A. Kojima et al. expected that the radial particle flux can be suppressed when the weak electric field forms in the core region and strong one forms in the peripheral region [16]. It is expected that this radial electric field profile can be formed by changing the end plate resistance. However, the relation between the radial profiles of the electric field and the fluctuation was not studied.

One of the most important issues in the magnetic confinement plasma is resolution of anomalous transport which is caused by turbulence fluctuations. The enhancement or suppression of fluctuation with existence of E×B has been observed in various devices. Therefore, potential and electric field control is effective method to fluctuation control. Potential control experiments have been carried out in GAMMA10. In these experiments, the relationship between electric field and density fluctuation was discussed. However, the simultaneous measurement of the potential and density fluctuation is important to study the mechanism of transport since the radial particle flux depends on the potential and density fluctuation. This thesis have the objected of studying the relation between the potential formation and the low frequency fluctuations by using gold neutral beam probe which measure the potential and density fluctuation simultaneously. The relation between the potential and the fluctuation is studied by using two kinds of methods for the potential formation control.

Firstly, central potential was increased in radial core region due to confinement potential formation by applying the plug ECH. Suppression of the drift-type fluctuation due to the plug ECH injection has been observed in the past studies [11,12]. Here, the relation between the suppression of the fluctuation and the radial potential and electric field formation is studied.

Secondly, central potential is increased in projected region of target due to the insertion of the target plate in the end region. It is known that sheath potential differs with the plate material [27,28]. The effect of materials on the potential formation by using carbon and tungsten as target plate is studied. In addition, it is expected that the radial particle flux which is driven E×B drift can be suppressed when the weak electric field forms in the core region and strong one forms in the peripheral region [16]. The insertion of the low resistance plate is effective to form that electric field since the central potential become high and almost constant in the projected region of the plate. In this thesis, the potential formation with the insertion of the target and the flute type fluctuation driven E×B drift and the behavior of the potential formation and the low frequency fluctuations are studied.

The outline of the paper is as follows. Experimental setup is explained in the Section 2. Result and discussion of fluctuation suppression with radial electric field by applying ECH and core plasma control with target plate insertion in end region are presented in the Section 3.1 and 3.2, respectively. And summary is given in Section 4.

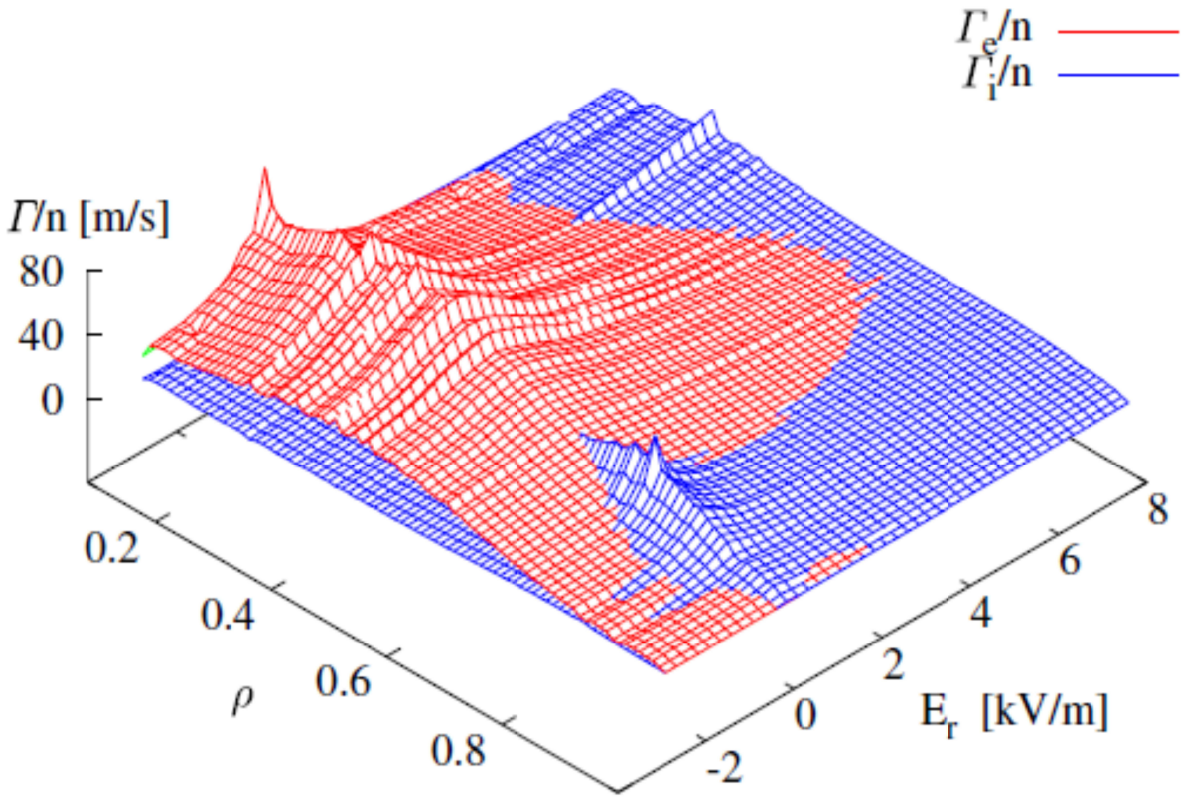

Fig. 1.1. Radial profile of the solution of the ambipolarity equation for the ECH plasma on TJ-II stellarator. ρ is radial position and Γ/n is normalized particle flux in the Figure. The electric field was controlled by electron cyclotron heating systems.

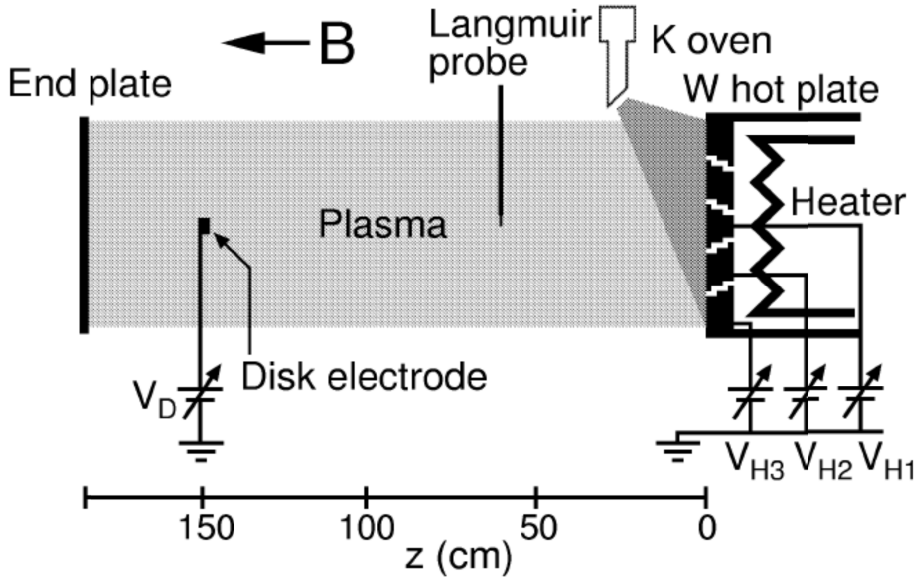

Fig. 1.2. The schematic of experimental setup on Q_T-Upgrade machine. The plasma potential at a different radial position can be independently controlled by the voltage applied to each segmented hot plate. This radially-different plasma potential, or the radial electric field E_r, gives rise to an $E_r \times B$ drift flow and its shear perpendicular to the magnetic field lines.

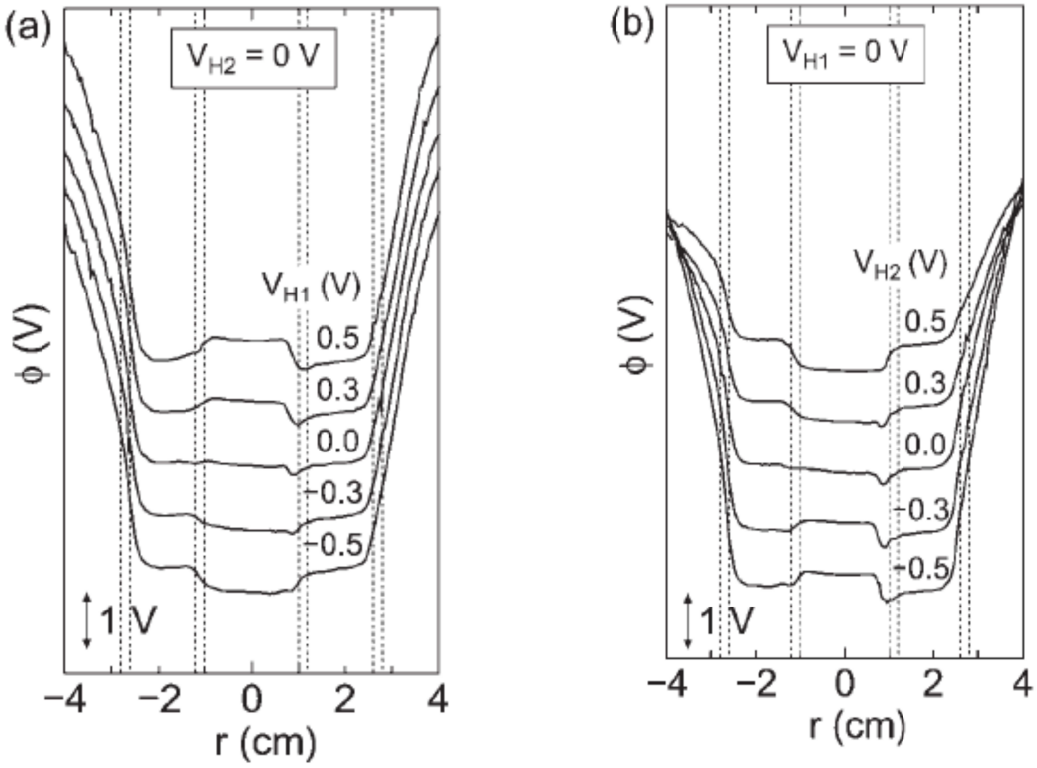

Fig. 1.3. Radial profiles of plasma potential (a) with V_{H1} as a parameter for V_{H2} = 0 V and (b) with V_{H2} as a parameter for V_{H1} = 0 V at z = 60 cm for B = 3 kG.

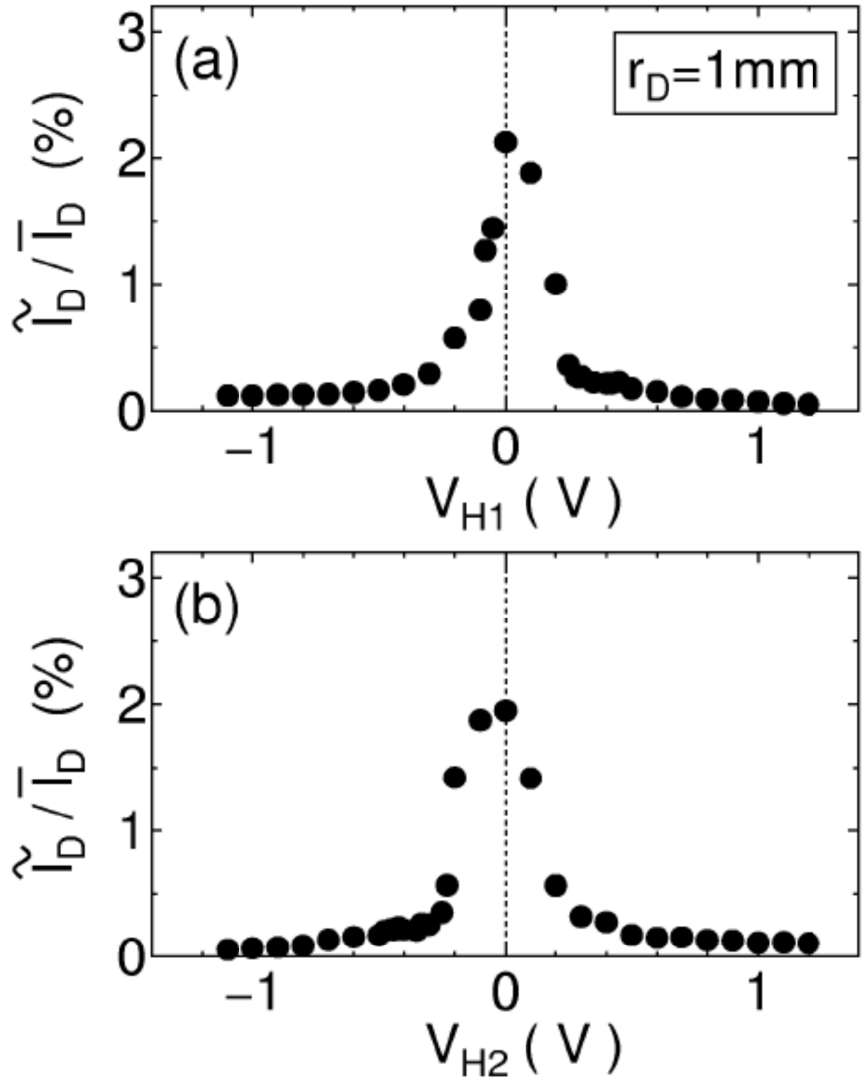

Fig. 1.4. Normalized ion cyclotron fluctuation amplitudes of the small disk electrode (as shown in Fig. 1.2.5) at r = 0 cm for V_D = 90 V (a) as a function of V_{H1} in the case of V_{H2} = 0 V and (b) as a function of V_{H1} in the case of V_{H1} = 0 V. The ion cyclotron instability excited in the case of almost no perpendicular shear for V_{H1} = 0 V is gradually suppressed with an increase or a decrease in V_{H1} as shown in (a). This suppression of the ion cyclotron instability is also observed with an increase or a decrease in V_{H2} as shown in (b).

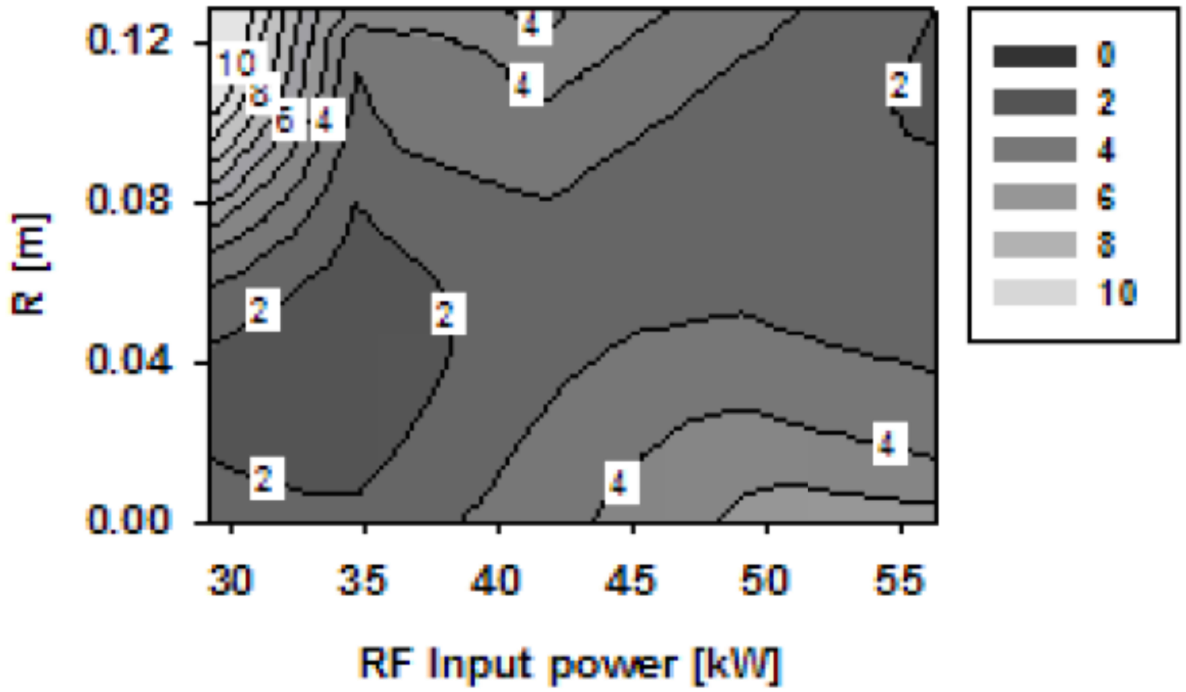

Fig. 1.5. The radial profiles of the potential fluctuation level in various RF powers on GAMMA10. This fluctuation was identified as the drift type fluctuation.

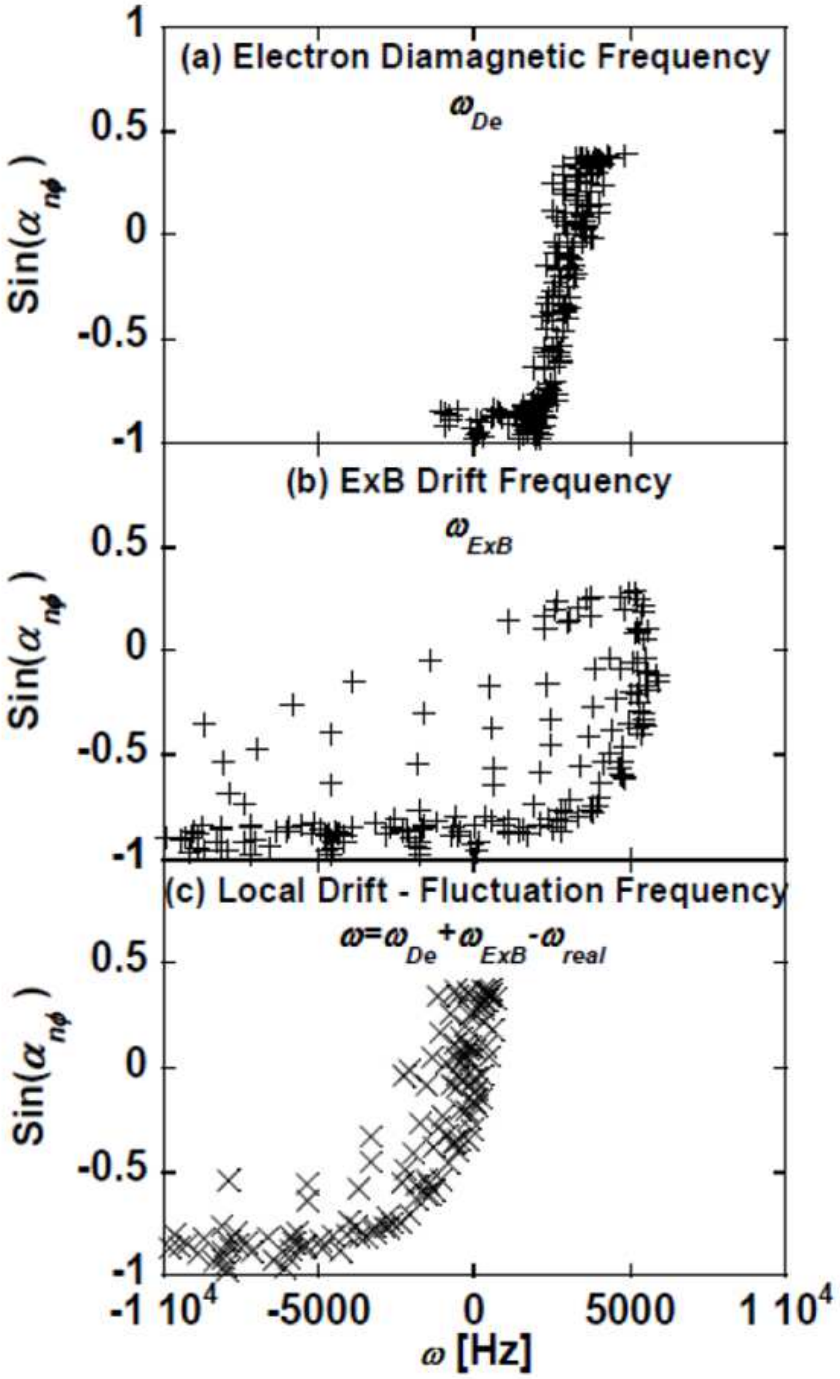

Fig. 1.6. The dependence of $\sin(\alpha_{n\varphi})$ on the frequency parameters, (a) the estimated electron diamagnetic drift frequency ω_{De}, (b) the estimated E×B drift frequency $\omega_{E\times B}$ and (c) $\omega_{De} + \omega_{E\times B} - \omega_{real}$, which ω_{real} is the observed frequency. When the value of $\omega_{De} + \omega_{E\times B}$ is equal to ω_{real}, $\sin(\alpha_{n\varphi})$ becomes zero. That is, the source of the drift type fluctuation is located at the position $\sin(\alpha_{n\varphi}) = 0$ (i.e. $\Gamma_p = 0$).

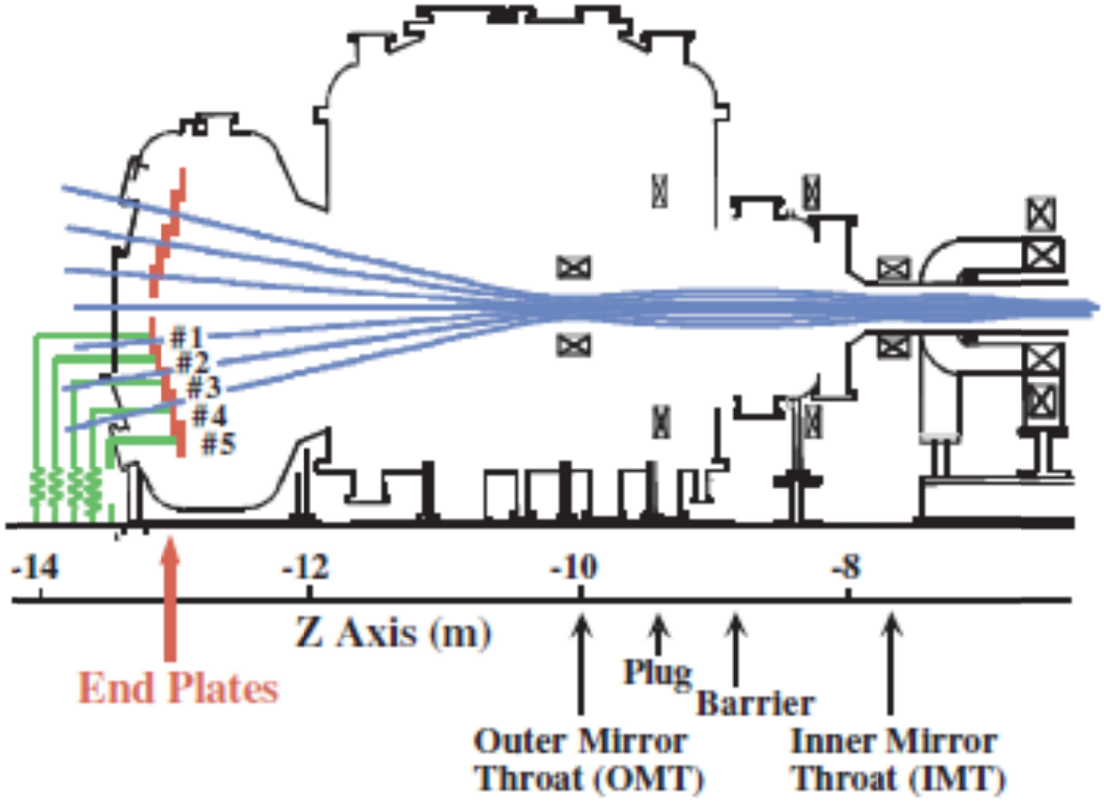

Fig. 1.7. Location of the end plates and the magnetic field lines on GAMMA10. The end plates are installed in front of both end walls on tandem mirror, they are coaxially divided into 5 portions numbered 1, 2, 3, 4, and 5. Usually, each end plate is grounded through the resistance of 280 kΩ, therefore, the plate potential indicates almost floating potential, therefore, the plate potential indicates almost floating potential. This potential was self-biased negatively due to inflow of the end loss electron. A voltage bias is applied to the plates #1 to 3.

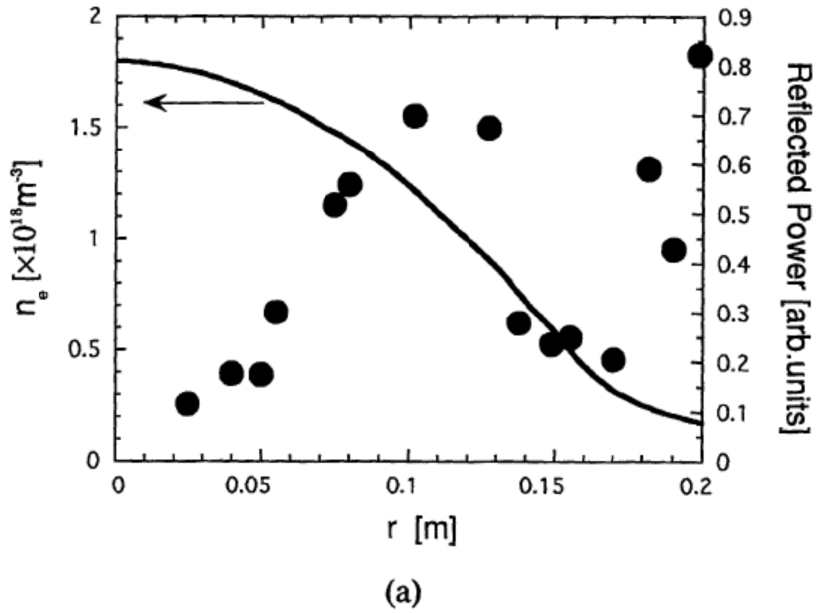

(a)

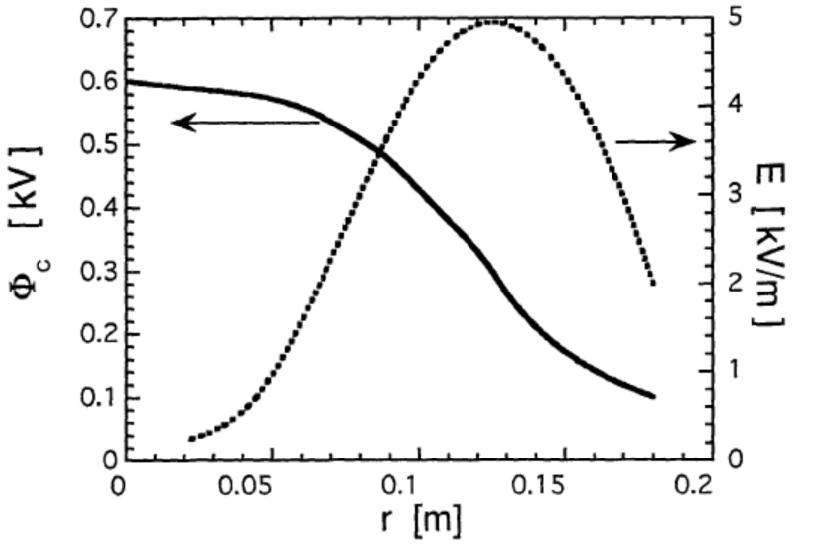

(b)

Fig. 1.8. (a) Radial profiles of the fluctuation level measured with a reflectometer and of the density for bias voltage V_B = 1 kV, (b) Radial profiles of the central potential Φ_c (solid line) and the electric field E_r (dotted line). It is seen that the fluctuation level is enhanced in the region of large electric field. The fluctuations of the coherent spectrum are driven by the E×B rotation.

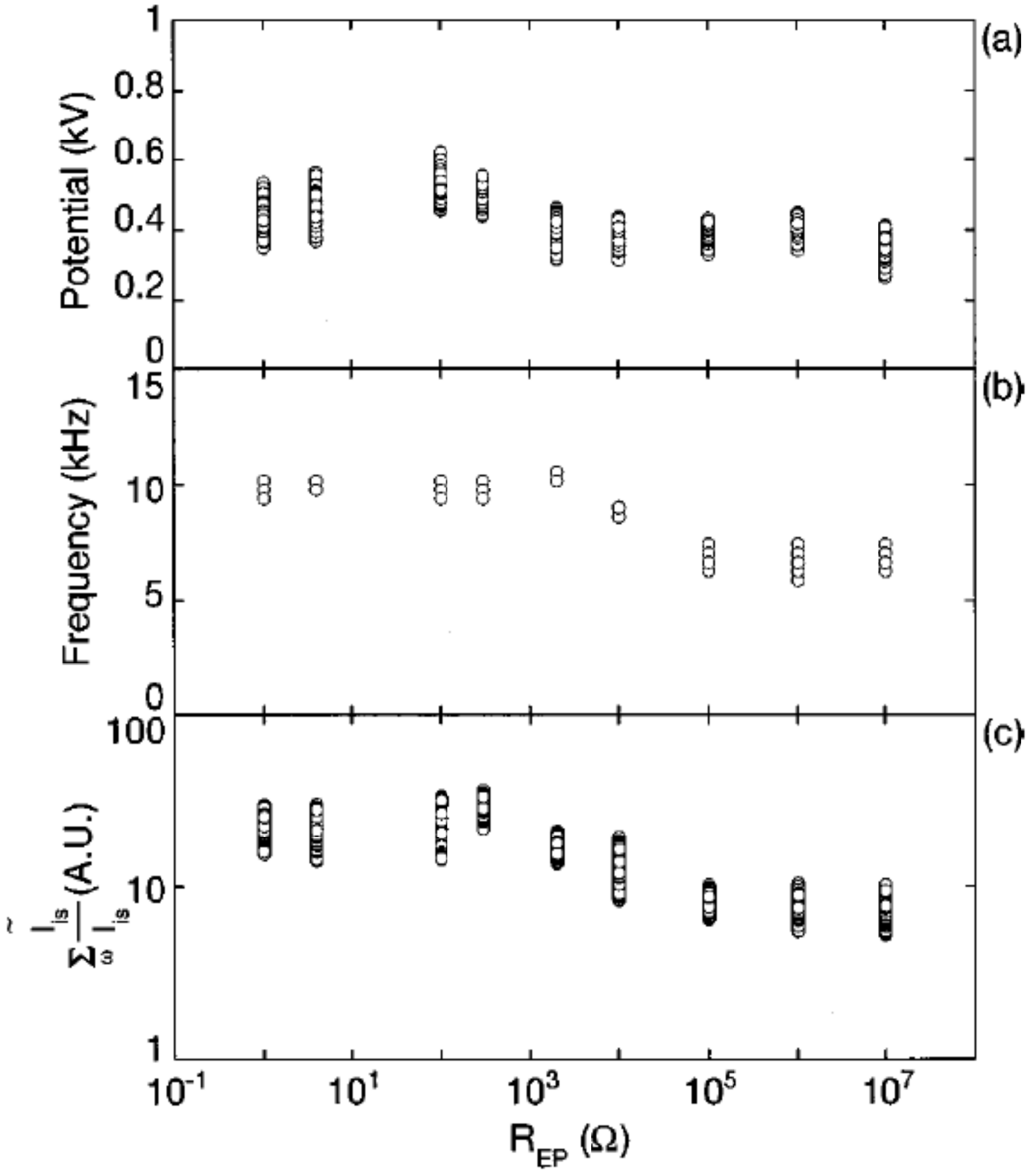

Fig. 1.9. The resistance of the end plate R_{EP} dependencies of (a) the potential in the central cell, (b) the frequency of the fluctuation, and (c) the amplitude of the fluctuation. When the resistance of end plate R_{EP} is decreased, the central potential Φ_c increases and fluctuations appear. When the resistance smaller than 10 kΩ is connected, the amplitude of the fluctuation increases and their frequency becomes higher.

2. Experimental Setup

2.2. GAMMA10

A moving charged particle experiences a Lorentz force in magnetic field. Lorentz force causes a particle to corkscrew along a magnetic field line. This motion has a Larmor radius which is the radius of the circular motion of the charged particle.

A charged particle in magnetic plasma has a magnetic moment. The magnetic moment is given by

$$\mu = \frac{m v_{\perp}^2}{2B}, \qquad (2.1)$$

where m is a particle mass, $v_{\perp}$ is a perpendicular velocity and B is magnetic field. In a magnetic mirror, as a charged particle moves along a magnetic line, it can enter a region of denser magnetic field lines. A particle experiences a force as following because of adiabatic invariance of the magnetic moment,

$$F = \mu \nabla B . \qquad (2.2)$$

This force F can reflect a particle. This mirror effect only occurs when a particle has the appropriate velocity and pitch angle.

GAMMA10 in university of tsukuba is a magnetic mirror device. The detailed information of GAMMA10 is presented later.

The simple mirror plasma is normally trapped due to the magnetic moment conservation. However, the particle with most of the kinetic energy in the parallel direction flows out to end region. To suppress these end loss particles, the ion confinement potentials and thermal barrier are formed at the plug/barrier cells. The ion confinement potentials trap low energy ions and the thermal barriers prevent the cold electrons from flowing in the confinement potentials.

Figure 2.1 shows a schematic view of GAMMA10, which is a tandem mirror device with minimum-B anchor and mainly separated into each sections, from the central to the end. In GAMMA10, the lengths of central, anchor and plug/barrier cells are 6.0 m, 4.8 m and 2.5 m, respectively. Magnetic field strength at the mid-plane of the central cell in which main plasma is produced and heated is about 0.41 T in a standard operation, and mirror ratio is 5. The anchor cells which suppress the magneto-hydro-dynamic (MHD) instability are located at the both sides of the central cell and consist of minimum-B mirror field which is produced by a base ball coil. The magnetic field strength is 0.61 T at the mid-plane of the anchor cell and mirror ratio is 3. The plug/barrier cells are located at the both ends of GAMMA10, where the electron and ion confinement potentials are produced. The axial profiles of the magnetic field strength and the schematic electrostatic potential on GAMMA10 are also shown in Fig. 2.1.

The initial plasma is produced by plasma guns (PG) which installed at the both ends on GAMMA10. And the gas puffing systems (GP) which inject the hydrogen gas are used for keeping and fueling the plasma. After starting up the plasma with the PG, the ion cyclotron heating (ICH) is used for the plasma production and heating. The ion

and electron axial confinement potentials are generated by using electron cyclotron heating (ECH) at the plug/barrier cells. They are called the plug potentials and the thermal barrier potentials

2.2. Heating systems

2.2.1. Ion cyclotron heating (ICH)

After starting up the plasma with the PG, the ion cyclotron heating (ICH) is used for the plasma production and heating. There are two types of oscillators named RF1 and RF2, and two types of antennas named the Nagoya type-3 and the double half turn antennas. Normally, the RF1 systems with the frequency of 9.9 MHz are connected to the Nagoya type-3 antennas and the RF2 systems with the frequency of 6.36 MHz are connected to the double half turn antennas. The RF1 frequency is equal to the ion cyclotron frequency at midplane of the anchor cell, the RF1 systems have roles of plasma heating at the anchor cell and plasma stabilization. The RF2 frequency is equal to the ion cyclotron frequency at midplane of the central cell, the RF2 systems heat central plasma.

2.2.2. Electron cyclotron heating (ECH)

In GAMMA 10, the electron cyclotron heating (ECH) systems produce the confinement potentials in plug/barrier cells. The ECH systems with the gyrotrons of the frequency 28GHz are installed. In the plug region, the resonance layer is located at the magnetic field strength of 1T, that is, the fundamental ECH is applied for producing the warm electrons. Then the warm electrons are accelerated along the magnetic field line by magnetic field gradient and the positive potential is formed.

2.2.3. Neutral Beam Injection heating (NBI)

The neutral beam injection (NBI) is a system to generate the high energy ions by use of high energy neutral particle. The sloshing and pumping NBI systems are installed in east and west plug/barrier cell, and the beam intensity is 25 keV and 70 A. The sloshing NBI systems product trapped ion distribution called “sloshing distribution”. The maximum and minimum of this distribution are located at turning point and midplane, respectively. This distribution contributes the confinement potential formation. The pumping NBI systems have role of the pumping cold ion from barrier cell.

2.3 Diagnostics

2.3.1. End Loss Ion Energy Analyzers (ELIEA)

End Loss Ion Energy Analyzers (ELIEA) has been installed at end to obtain the plug potential and the structure of the ion distribution in the loss region. ELIEA consists of secondary electron repeller grid, ion repeller grid and collector plate as shown in Fig. 2.2. The incident ion energy E is analyzed by an applied bias V on the ion repeller grid, that is, the ions with $E < eV/\cos\theta$ are repelled by the ion repeller grid bias and are collected on a collector plate. Here, θ denotes the angle between the ion incident direction and the ion repeller grid surface, and the electronic charge is described as e. Incident electrons flow through slanted grid meshes, and then away through the exit mesh. Therefore, they are not collected on the collector plate. Further, the applied bias of negative

for the secondary electron repeller mesh retards secondary electrons from the grounded collector plate and the other meshes.

2.3.2. Gold Neutral Beam Probe (GNBP)

2.3.2.1. Principle of beam probe

Beam probes are useful tools for the plasma potential measurement. A lot of beam probe systems have been constructed and widely used. The beam probe is active measurement method, and does not influence to plasma. One is the beam source which produces a high energy ion beam and the other is a beam detector by the use of an electrostatic energy analyzer. The incident beam is named primary beam, and the ionized ion beam is named secondary beam. The plasma potential is estimated from the change of the beam energy as follows:

$$\Phi = \frac{1}{Ze}\left(E_{secondary} - E_{primary}\right), \qquad (2.3)$$

where $E_{primary}$ and $E_{secondary}$ are the energy of the primary and secondary beams, Z is the change of the ion charge number at ionization point, Φ is the plasma potential at the ionization point. The ionization point of the secondary beam is limited due to the slit in front of the analyzer. Therefore the electrostatic potential at the ionization point is measured with beam probe.

2.3.2.2. Feature of GNBP in GAMMA10

Features of the gold neutral beam probe (GNBP) system on GAMMA 10 are described. Figure 2.3 shows a schematic view of the GNBP system. The notable features of GNBP are use of the neutral primary beam and the negative gold source by Cs sputtering. Those advantages are followings:

1. simplicity of maintenance of the beam source
2. no stable isotope (^{197}Au~100%)
3. large mass number
4. large sputtering yield
5. large cross-section of ionization from the primary (Au^0) to secondary (Au^+) beam
6. high neutralizing efficiency from the negative ions (Au^-) to neutrals (Au^0)
7. no influence of the magnetic field and the electric field on the primary beam

The isotopes and the magnetic fields cause the error of the potential measurement. There are the advantages to earn the high signal-to-noise ratio.

GNBP consists of three parts; an ion source, a neutralizer, and an analyzer. The gold negative ion is generated and accelerated in an ion source. The energy and the incident angle of the beam passing the plasma center is about 11.78 keV and 40 degrees, respectively. The GNBP system has two incident angle deflectors of the vertical and horizontal directions. In order to obtain the radial profile of the electrostatic potential, the primary beam is swept by the vertical deflector. A neutralizer is installed in between an ion source and GAMMA10 because the neutral beam has been employed as the primary beam. The ionized beam from an ion source collides with hydrogen and

neutralize in a neutralizer. An electrostatic energy analyzer is installed with the incident angle of about 45 degrees. In the analyzer, the micro-channel plate (MCP) detector of 32 anodes is utilized for the beam detection. The width of an each anode is 2.4 mm.

Principles and applications of the density, potential and magnetic field measurement are described. The beam diagnostic always has the problem caused by the beam attenuation. Because the primary and secondary beams pass through the plasma, the beams are affected by some interactions. In the density measurement, the beam currents are attenuated by the plasma until the secondary beam is detected.

Because the neutral beam is utilized as the primary beam, only the secondary beam is affected by the electric and magnetic field, that is, the ionization point (measurement point) is on the straight line of the primary beam. Then, the ionization point and the beam trajectory are described by some parameters which are the magnetic field, the incident angle, the particle mass, the beam energy, the beam slit position and the plasma potential. Therefore, there is a possibility of the shift of the ionization point due to the change of the plasma potential.

Figure 2.4 shows the measuring range of GNBP. The ionization point (measurement point) shifts in the direction of the straight line of the primary beam when the beam energy changed. In addition, the ionization point depends on the beam incident angle (i.e. depend on the beam deflector voltage). Therefore, GNBP can measure spatial distribution by changing beam energy and deflector voltage as shown in Fig. 2.4.

One of the advantages of the beam probe is that it can measure potential fluctuation and density fluctuation simultaneously. The potential fluctuation level is calculated as amplitude of the measured potential. The calculation method of the density fluctuation level will be described later.

The detected secondary beam is derived from the primary beam ionized at the ionization point. The electron-impact ionization process is dominant in a case of the ionization of the primary beam. Therefore, the secondary beam current depends on the electron distribution function. If the electron distribution function is assumed to be Maxwellian, the electron density and temperature can be explained. The numerical expression of the cross-section σ is as follow:

$$\sigma(E) = a\frac{\ln(E/P_i)}{EP_i}\{1 - b\exp[-c(E/Pi) - 1]\}, \qquad (2.4)$$

where E is the electron energy, P_i=9.23 eV is the first ionization potential, a, b and c are the atomic inherent constants, $(a,b,c) = (7.6\times10^{-17}, 1.5, 0.18)$, respectively. The expression of the ionization rate coefficients S is as follow:

$$S(T_e) = 3.0\times10^{-12}\frac{\xi_i}{P_i\sqrt{T_e}}\int_{P_i/T_e}^{\infty}\frac{\exp(-x)}{x}dx. \qquad (2.5)$$

Here ξ=25 is the number of the equivalent electrons of the atom, T_e is electron temperature in unit of eV. The ionization process from the most other shell is assumed to be dominant. The ionization rate Q can be written as

$$Q = \frac{n_e \langle \sigma v \rangle}{v_b} = \frac{n_e S}{v_b}, \qquad (2.6)$$

where v_b is the velocity of the beam. Therefore, the secondary beam current depends on both the electron density and temperature. The beam current depends on the electron density linearly. Now, the dependence on the temperature is examined. The total differential of the ionization rate can be written as

$$\begin{aligned} dQ &= \left(\frac{\partial Q}{\partial n_e}\right) dn_e + \left(\frac{\partial Q}{\partial T_e}\right) dT_e = \left(\frac{S}{v_b}\right) dn_e + \left(\frac{n_e}{v_b}\frac{\partial S}{\partial T_e}\right) dT_e \\ &= n_e \left\{ g_n \frac{\Delta n_e}{n_e} + g_T \frac{\Delta T_e}{T_e} \right\} \\ &= n_e g_n \left\{ \frac{\Delta n_e}{n_e} + \frac{g_T}{g_n} \frac{\Delta T_e}{T_e} \right\} \end{aligned} \quad , \qquad (2.7)$$

where the dependence factor g are defined as follow:

$$g_n = \frac{S}{v_b}, \qquad g_T = \frac{T_e}{v_b}\frac{\partial S}{\partial T_e}. \qquad (2.8)$$

Therefore, the rate of the differential of the secondary beam current per itself is written as

$$\frac{dI}{I} = \frac{dQ}{Q} = \frac{\Delta n_e}{n_e} + \frac{g_T}{g_n}\frac{\Delta T_e}{T_e}. \qquad (2.9)$$

Then the dependence factor g_t is calculated as follow:

$$g_T = \frac{T_e}{v_b}\frac{\partial S(T_e)}{\partial T_e} = \frac{3.0\times10^{-12}}{v_b}\frac{\xi_i}{P_i T_e^{1/2}}\left\{ \exp(-P_i/T_e) - \frac{1}{2}\int_{P_i/T_e}^{\infty} \frac{\exp(-x)}{x} dx \right\}. \qquad (2.10)$$

Then the ratio of the dependence factors can be written as

$$\frac{g_T}{g_n} = \frac{\exp(-P_i/T_e)}{\int_{P_i/T_e}^{\infty} \{\exp(-x)/x\} dx} - \frac{1}{2}. \qquad (2.11)$$

The ratio is almost zero in the electron temperature region of GAMMA 10. (For example, the ratio is about +0.06 and -0.003 with T_e = 50 eV and 100 eV, respectively.) Therefore it is found that the secondary beam current is

more sensitive to the electron density than the electron temperature. The beam current fluctuation is dominant to be the density fluctuation.

2.3.2.3. Calibration

The coordination of the primary beam changes with time, because it of the gold target which produces the gold negative ion changes with time. The primary beam is adjusted as the convergence and the acceleration. The primary beam is focused by the use of Focus Lens and Einzel Lens. The shift of the primary beam is detected with Faraday Cup No. 4 (FC4) placed opposite the ion source. FC4 consists of the cupper 9 plates, and each plate can detect the beam signal independently. The primary beam to the convergence by modulating an applied voltage of Einzel Lens is calibrated by the use of FC4. In addition, the primary beam can be deflected vertical (X direction) and Z direction by two kinds of the deflection plates. The vertical deflection plate is called “deflector”, and the Z direction deflection plate is called “steerer”. The optimal applied voltage to the deflection plate by deflecting the primary beam parallel and perpendicularly is resolved by calibration data of FC4.

The applied voltages of each deflection plates that the primary beam passes through the center position in GAMMA 10 were calibrated. Then, the ionization point was also calibrated. The potential profile is measured by deflecting the primary beam by the use of vertical sweeping deflector. The Faraday Cup 3 (FC3) is inserted from the top in GAMMA 10 for obtaining the relationship between the applied voltages of deflector and ionization point. FC3 consists of the cupper 5 plates, and each plate can detect the beam signal independently. It is possible to detect the primary beam directly and obtain optimal applied voltage to the inserted position.

The relationship between the plasma potential and the flying distance of secondary beam on the analyzer was calibrated. The secondary beam has the information of the plasma electrostatic potential because it obtained plasma potential energy on the ionization point. Normally, GAMMA10 experiments is carried out on order of 10^{-7} Torr, although, the calibration experiment is carried out on order of 10^{-5} Torr in the central cell. The magnetic field distribution in calibration agrees it in normal experiments. The gold neutral beam is ionized by collision with N_2 (or O_2) at the ionization point. The beam energy is not change in this case since the plasma does not exist. So, the primary beam has the acceleration energy and the additional energy accelerated by the ion source as virtual potential. The relationship between the virtual potential and the flying distance of the secondary beam in the analyzer is obtained. The flying distance of the secondary beam is detected as the channel distribution of the beam signal at the micro channel plate. The beam signal is measured by count mode since the ionized beam current is very few. Then, the peak channels of beam signal in the calibration experiment are obtained. The relational expression between the virtual potential and the flying distance of secondary beam as the channel distribution of the beam signal at the micro channel plate from the calibration experimental results is employed to plasma experiments as calibration formula.

Figure 2.5 shows the channel distribution of beam signal in the calibration experiment. The red circles and blue squares correspond to the beam signals with virtual potential 0 V and 400 V. The potential calculating formula that the arguments of function are the ionization point and the peak channel of the beam intensity is obtained. The peak channel is the channel number of the micro channel plate in which the maximum current signals. Figure 2.6 shows the relationship between the virtual potential and the flying distance of secondary beam as the peak channel distribution at R = 0 cm. The calibration formula in the direction of beam line is obtained by

currying out same operations at R_{BL} = 0 - 12 cm. On the other hand, the calibration formula in the X direction is obtained as shown in Fig. 2.7. I found the potential derivation formula of the radial profile from Fig. 2.7 as follows;

$$\phi(x) = \frac{P_{ch} - \left(22.008 + 0.057259x - 0.0071512x^2\right)}{0.015791 - 0.000022593x - 0.0000022978x^2}, \qquad (2.12)$$

where φ [V] is the electrostatic potential, x [cm] is the radial distance of the measurement point, and P_{ch} is the peak channel.

2.3.2.4. Channel profile of beam signal

The channel profile of beam signal is asymmetric as shown in Fig. 2.5. The beam has width in the direction of $R_{\perp}$ as shown in Fig. 2.8. The incident angle into the analyzer differs depending on the ionization point. The relationship between $R_{\perp}$ and the incident angle was estimated by beam trajectory calculation as shown in Fig. 2.9. The relationship is presented as following formula;

$$\theta = 0.367R_{\perp} + \theta_0, \qquad (2.13)$$

where θ_0 is the incident angle of beam center. The beam probe in GAMMA10 was designed as θ_0 = 45°. The flying distance in the analyzer is presented as follows;

$$\frac{2hE_b}{V_a}\sin 2\theta = L + N_{ch}d, \qquad (2.14)$$

where E_b is beam energy, V_a is deflecting voltage in analyzer, h is distance between deflecting electrodes, L is distance between beam slit and MCP, N_{ch} is channel number of MCP, and d is width of a channel. The channel number N_{ch} bears a proportionate relationship to sin2θ. If the relationship between the beam amount and $R_{\perp}$ is assumed as a Gaussian with HWHM 1 cm, the relationship between the beam amount and sin2θ can be presented as shown in Fig. 2.10. A sin2θ corresponds to the flying distance or the channel number. However, the calculated beam profile as shown in Fig. 2.10 is not similar to experimental it as shown in Fig. 2.5. Here, it is assumed that the incident angle of beam center θ_0 is 44° (or 46°). Figure 2.11 shows the calculated beam profile in the case of θ_0 = 44°. The beam profile as shown in Fig. 2.11 is similar to it as shown in Fig. 2.5. These results show that the asymmetry of the experimental beam profile arises from the beam width and the incident angle gap.

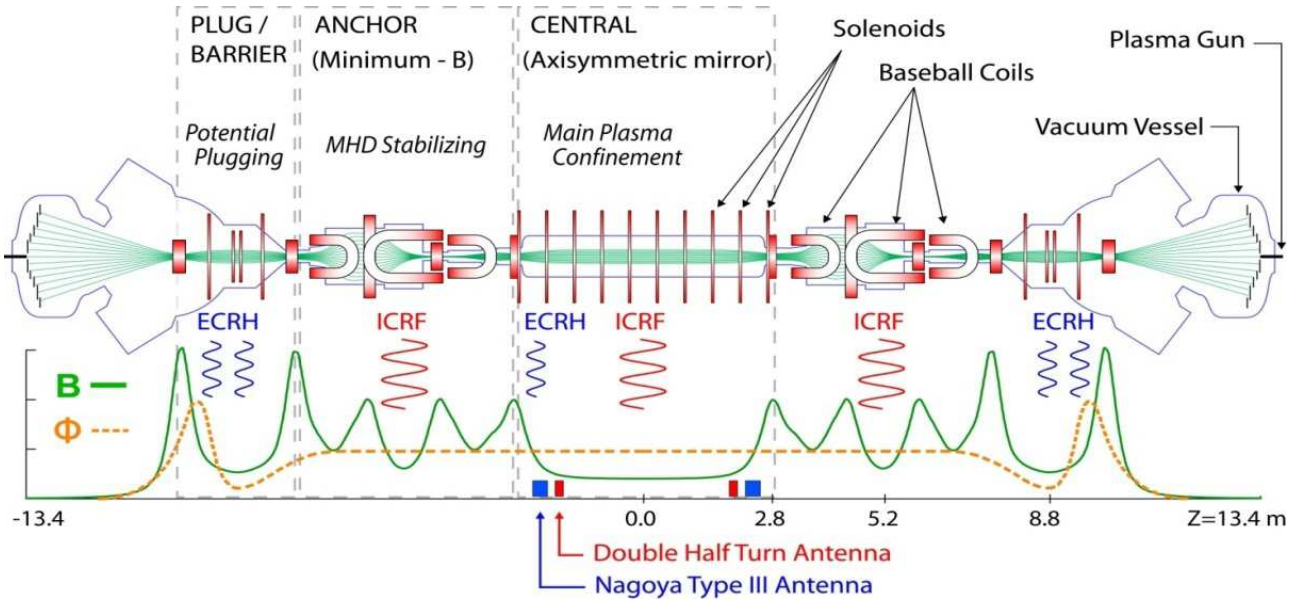

Fig. 2.1. The schematic of tandem mirror GAMMA10. The solid line and dotted line are the axial profiles of the magnetic field strength and the schematic electrostatic potential, respectively.

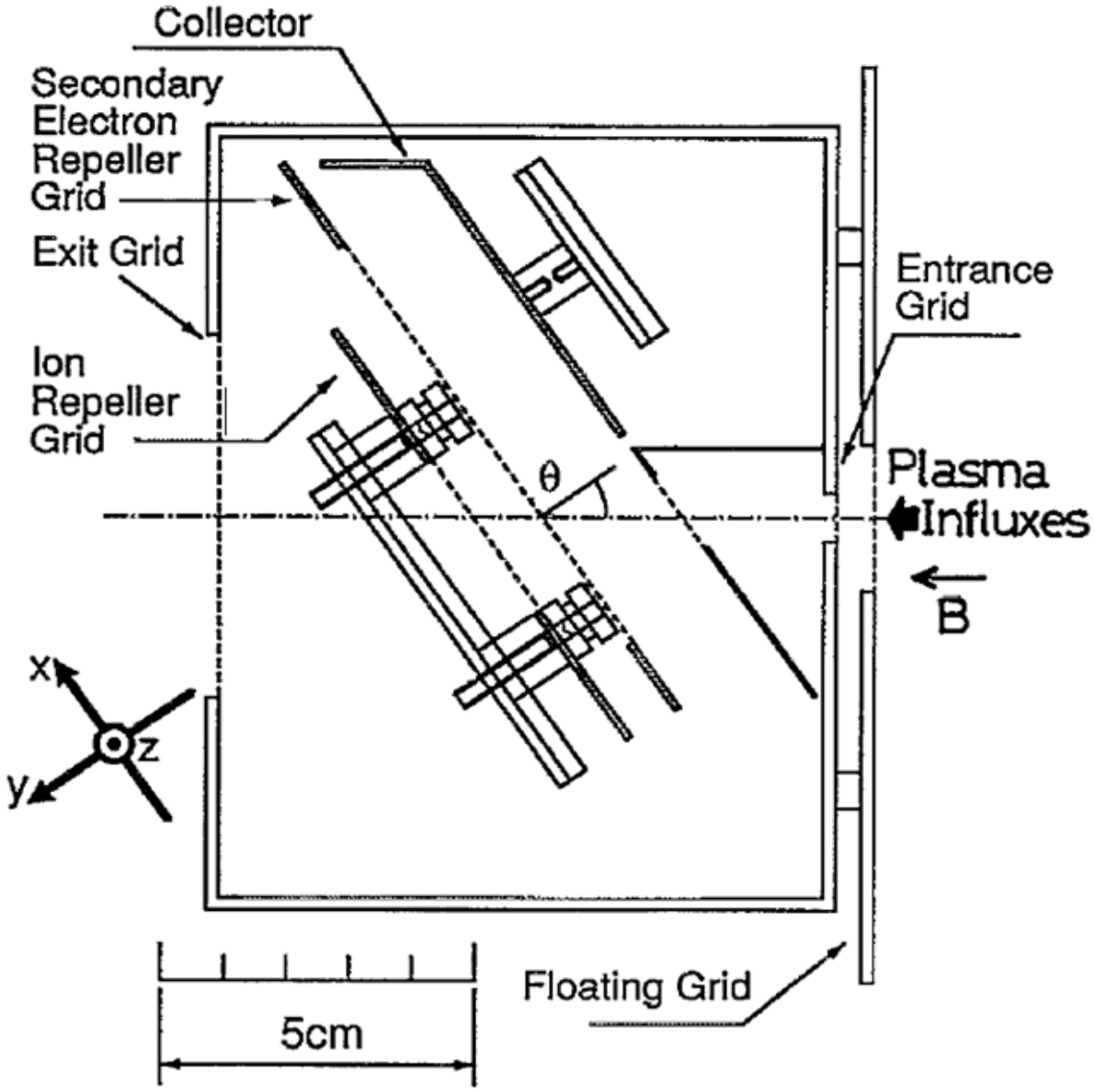

Fig. 2.2. The schematic of End Loss Ion Energy Analyzer (ELIEA). ELIEAs are installed behind end plates. Plasma flux came into the device from right side of figure.

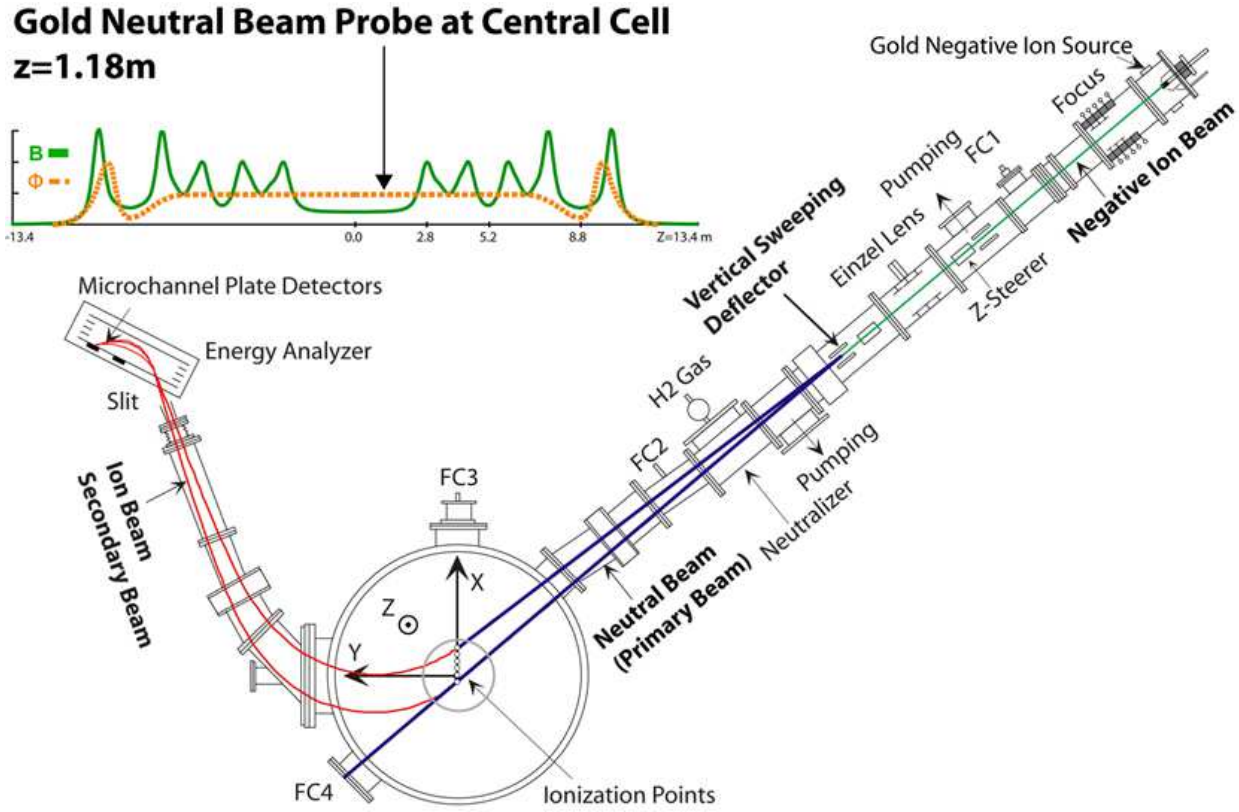

Fig. 2.3. The Schematic of Gold Neutral Beam Probe (GNBP). GNBP is installed at Central Cell on GAMMA10. GNBP consist beam south (right side of figure) and detector (left side).

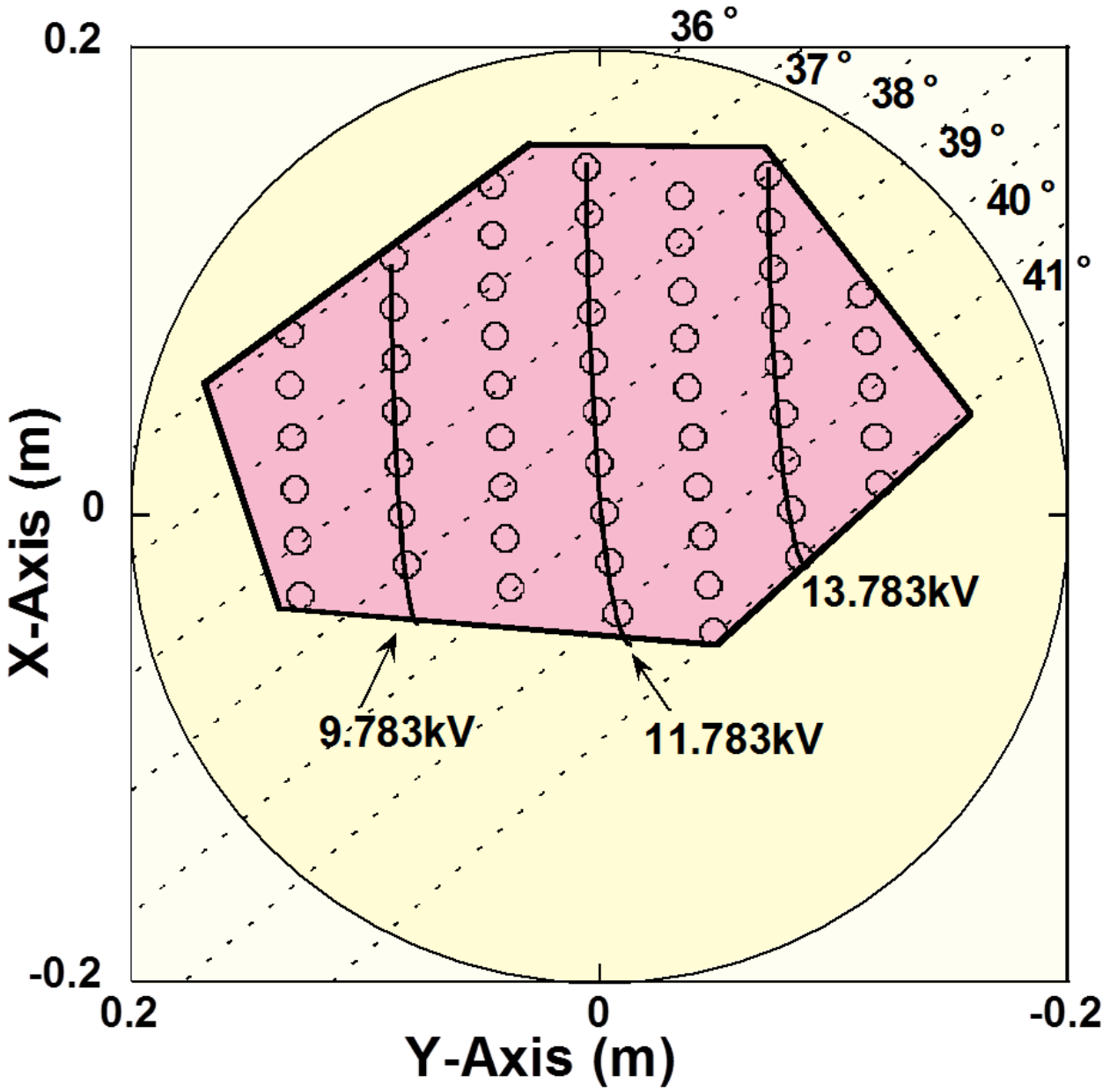

Fig. 2.4. The measuring range of GNBP. The ionization point (measurement point) depends on beam energy and incident angle.

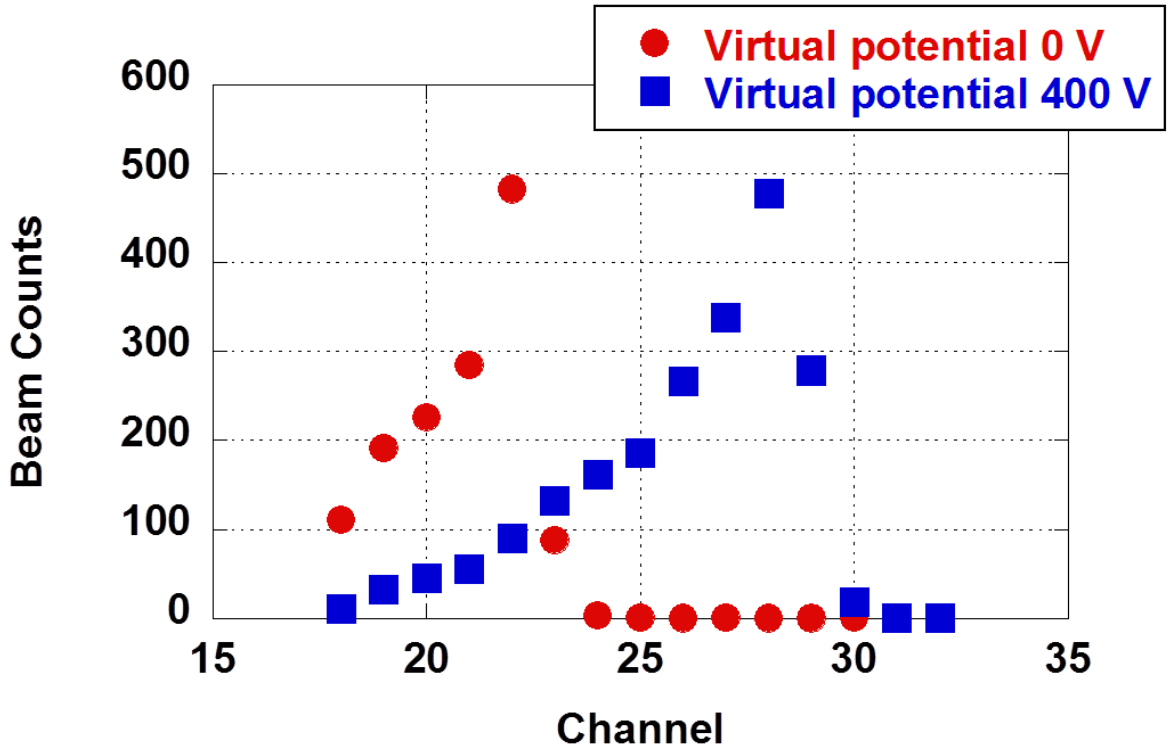

Fig. 2.5. The beam signal distributions with virtual potential 0 V and 400 V on the MCP channels. Peak channel is obtained from these distributions.

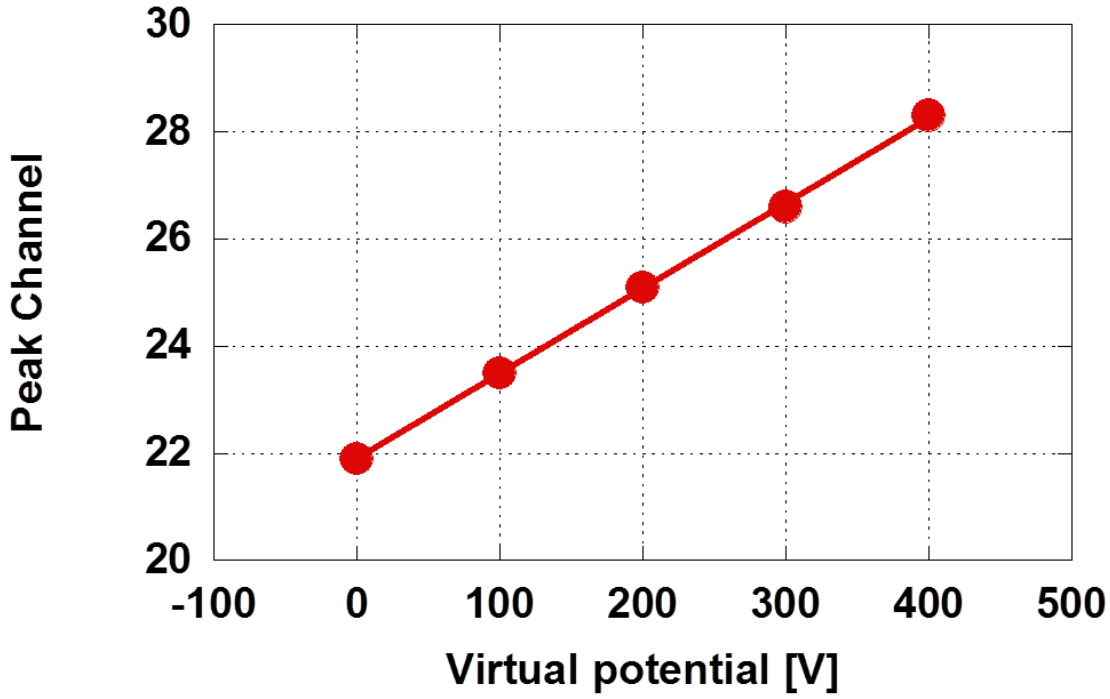

Fig. 2.6. The relationship between the virtual potential and the peak channel distribution at R = 0 cm.

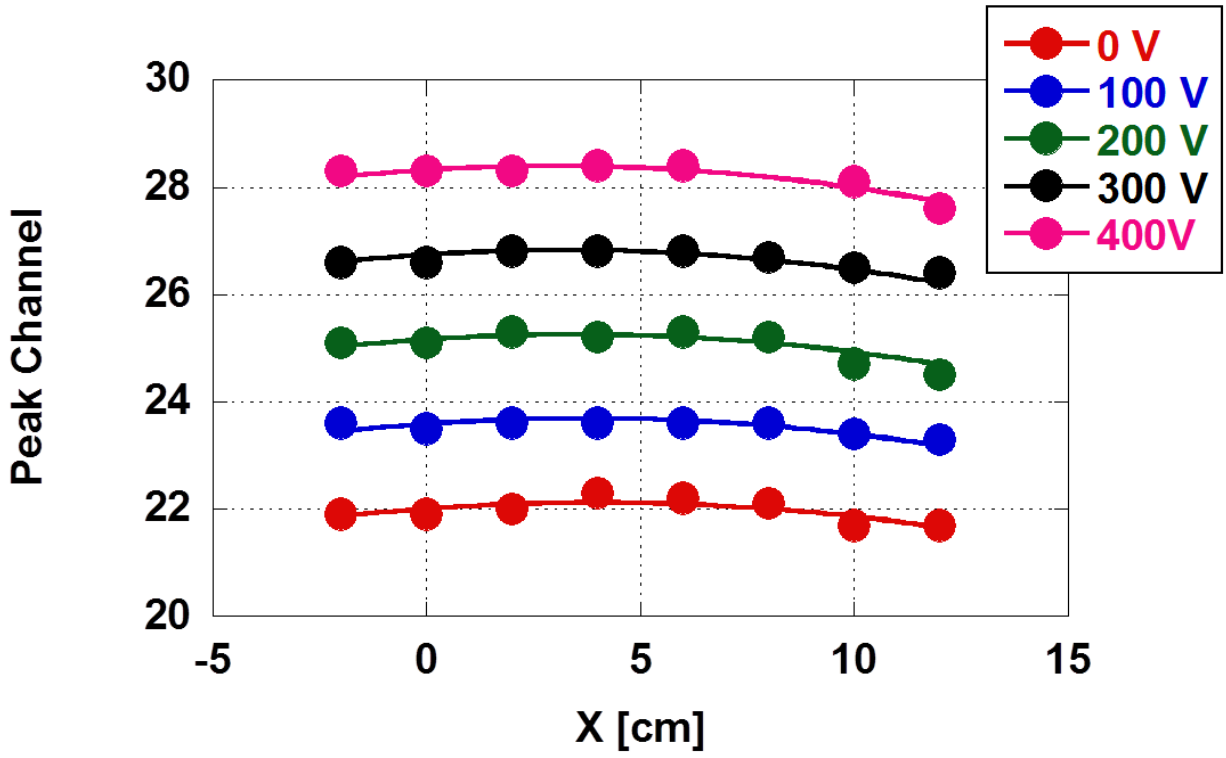

Fig. 2.7. The relationship between the radial position X [cm] and the peak channel distribution in each virtual potentials. The potential derivation formula is obtained from the calibration formula of this profile.

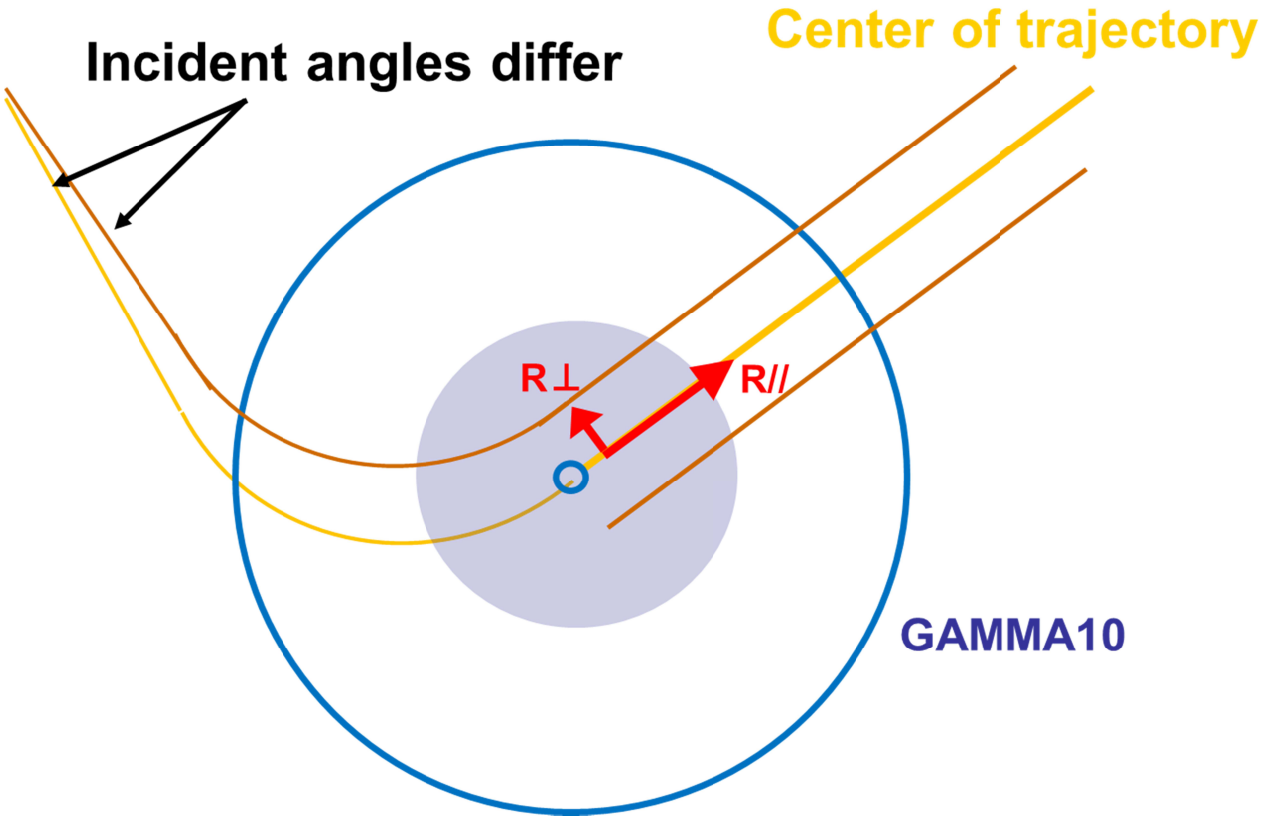

Fig. 2.8. The schematic of beam trajectory. The parallel and perpendicular direction to the primary beam line are defined as $R_{//}$ and $R_{\perp}$, respectively.

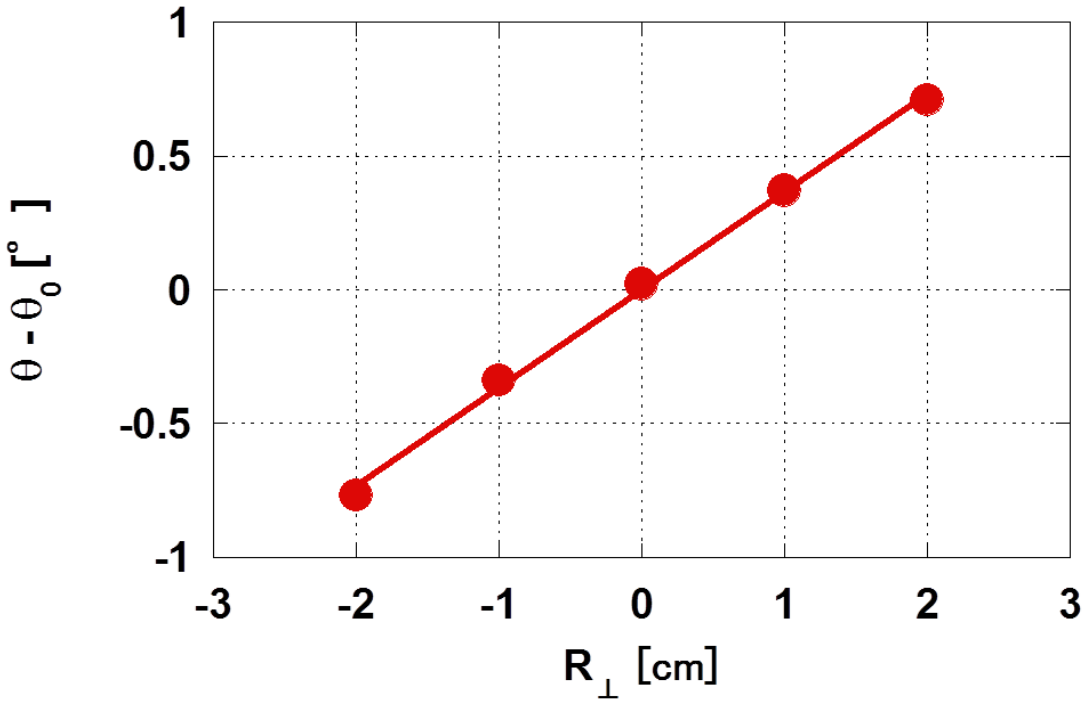

Fig. 2.9. The relationship between the incident angle gap and $R_{\perp}$. θ_0 is the incident angle of the center beam trajectory.

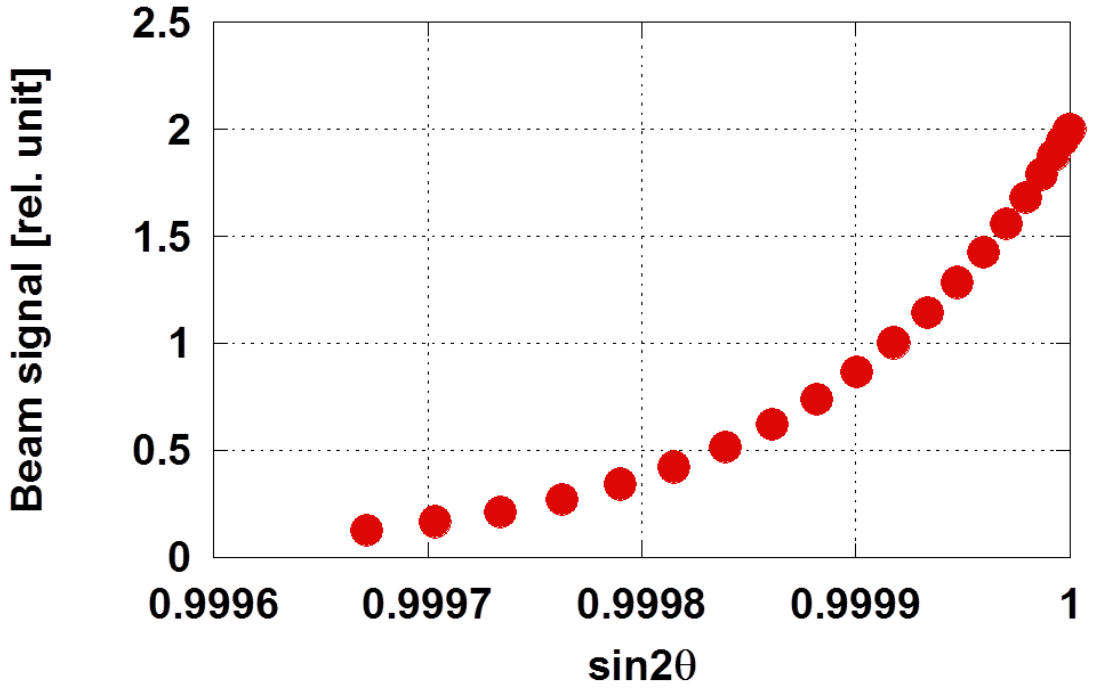

Fig. 2.10. The estimated relationship between the beam signal and sin2θ with $\theta_0 = 45°$. A sin2θ corresponds to the flying distance or the channel number.

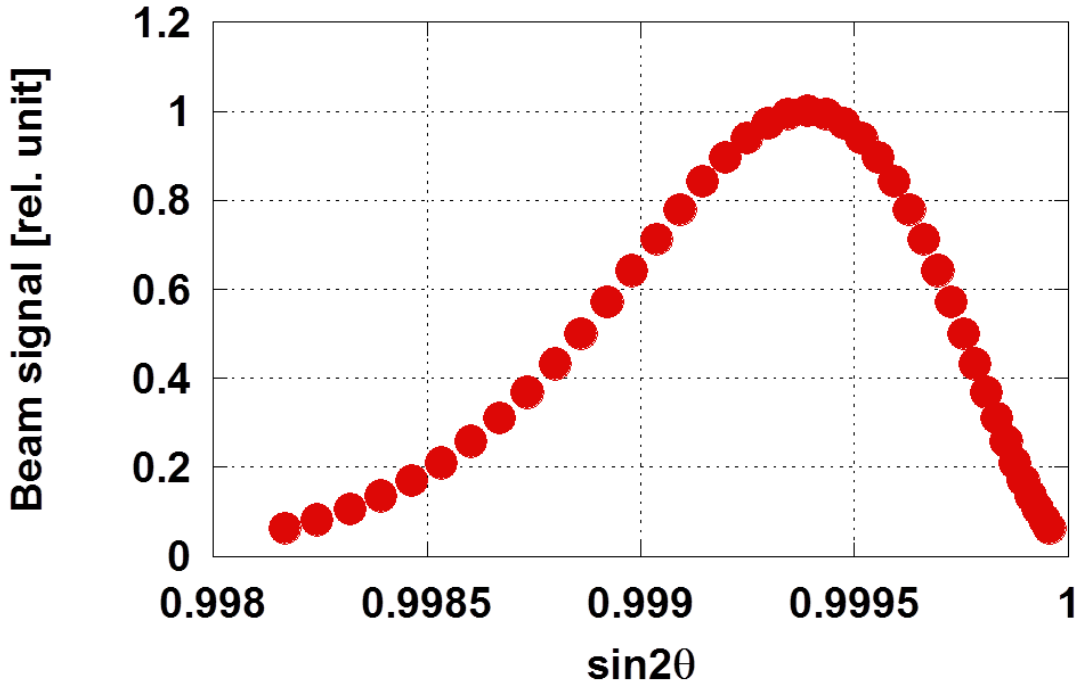

Fig. 2.11. The estimated relationship between the beam signal and sin2θ with $\theta_0 = 44°$.

3. Result and discussion

3.1. Fluctuation suppression experiment

In the GAMMA10, suppression of the drift type fluctuation has been observed when plug ECH is injected. This phenomenon has been studied [11,12]. The plasma was produced and heated by ICH. Central, barrier, and plug ECHs were applied. The time variation of plasma potential radial profiles in the central cell of GAMMA10 was measured by using GNBP. In order to obtain the radial distribution of potential at each period, the primary beam trajectory was deflected in the radial direction of 0–12 cm, and stationary measurement was carried out on shot by shot.

Figure 3.1.1 shows the time evolution of the line density and the diamagnetism of the central plasma (i.e. core plasma). The ICH was applied from 53 ms to 240 ms. The ECH was applied at the barrier region from 150 ms to 200 ms and at the plug region from 151 ms to 180 ms. The line density and the diamagnetism were maintained almost constant at 120-150 ms and then increased by the plug ECH. Here, a period in which the plasma was sustained by ICH only is called as “ICH period” and a period in which the plug ECH was applied is called as “ECH period”. Figure 3.1.2 shows the time evolution of the plasma potential at about R = 0 cm in the central cell. The potential was maintained almost constant at 120-150 ms and then increased to about 400 V by the plug ECH. The error of the potential measurement is also estimated to be about 15 V from the measurement error of the GNBP system in GAMMA10.

Figure 3.1.3 shows a radial profile of the potential, which was measured shot by shot. The potential increased during the application of plug ECH. The central-cell potential is estimated to be about 400 V at the center. Next, the radial potential fluctuation in the range of R = 0–12 cm was calculated by using the fast-Fourier-transform (FFT) calculation. The window function which was used in the FFT was the Hanning window, and the number of samples was 2048. Figures 3.1.4 and 3.1.5 show the radial profile of the potential and density fluctuation spectra in the ICH period and the ECH period, respectively. The characteristic fluctuation was observed at about 10 kHz as shown in Fig. 3.1.4. This fluctuation was identified as the drift type fluctuation. Then, the drift type fluctuation suppression with the application of the plug ECH was observed as shown in Fig. 3.1.5. The electric field shear in the ECH period was weak in R = 0-14 cm as shown in Fig. 3.1.3. So, strong electric field shear which is effective to suppress the drift type fluctuation may exist in R = 14-20 cm.

Figure 3.1.6 shows the radial profile of $\alpha_{n\varphi} = \alpha_n - \alpha_\varphi$ which is the phase difference of the density and potential fluctuations in the ICH period in this experiment. The radial particle flux Γ_p is estimated experimentally according to the following expression,

$$\Gamma_p = -\frac{2}{B_z}\int_0^\infty k_\theta(\omega)\left|\gamma_{n\phi}(\omega)\right|\tilde{n}(\omega)\tilde{\phi}(\omega)\sin\alpha_{n\phi}(\omega)d\omega, \qquad (3.1)$$

where k_θ is the azimuthal wave number, $\tilde{n}$ and $\tilde{\varphi}$ are the density and potential fluctuation levels, $\gamma_{n\varphi}$ is the coherence between the density and potential fluctuations, and $\alpha_{n\varphi}$ is the phase difference, respectively. Figure 3.1.7 shows the radial profile of normalized particle flux driven by the drift type fluctuation in the ICH period. When the drift type fluctuation was suppressed in the ECH period, this radial particle flux also disappeared.

The relationship between the electric field strength and the fluctuation level in the ICH period and the ECH period are shown in Fig. 3.1.8. It is seen that the electric field was positive when the suppression of the drift type fluctuation was occurred.

3.2. Target plate insertion experiment

In order to study relation between the potential structure and the low frequency fluctuations and relation between floating potential of plates in end region and the central plasma potential, a target plate was inserted at 543 mm from the exit of the west end coil (i.e. at Z = 10.74 m) in the west end region and it is grounded through the resistor as shown in Fig. 3.2.1. The material of the target plate was tungsten or carbon. The radius of the target plate is 5 cm and the projected radius at the central cell is about 4.1 cm. It is noted that the initial plasma was generated only by the east plasma gun in this experiment, since the target plate was inserted at the west end region.

It is known that the electrostatic potential of the end plates and the core plasma potential could be control by changing the ground resistances of end plates [23,25,26]. The central potential became high and almost constant in the projected region of the grounded plate. The ground resistance was changed for each plate. Radial profiles of plasma potential at the central cell in the cases of each resistance value of the end plates or the inserted target plate were observed by the GNBP.

Figure 3.2.2 shows the time evolution of the line density and the diamagnetism of the central plasma (i.e. core plasma). The ICH power was 160 kW and it was applied from 54 ms to 240 ms. The ECH power of 50 kW was applied at the plug region from 150 ms to 165 ms. The statistical errors of the line density and diamagnetism are 10% and 8%, respectively. The line density and the diamagnetism were maintained almost constant at 70-150 ms and then increased by the ECH. After the ECH was turned off, they decreased toward the original values.

Figure 3.2.3 shows the time evolution of (a) the potential of the target plate of carbon and tungsten and (b) the central plasma potential in the cases of the ground resistance of 80 Ω and 280 kΩ. As shown in Fig. 3.2.3(a), the target plate potential was decreased by the ECH in every case of the carbon and tungsten plates and low and high ground resistances. In the case of the ground resistance of 280 kΩ, the potential (i.e. floating potential) of the carbon target became negatively deeper than that of tungsten when the ECH was applied. On the other hand, there is no difference in the plate potential of the carbon and tungsten targets in the case of the ground resistance of 80 Ω. The reason of this behavior in the potential will be discussed in next section.

3.2.1. Secondary electron emission of target plate

The difference between the potential of carbon and tungsten targets in the ECH period is considered to be caused by the effective secondary electron emission. If the secondary electrons are emitted from the target plate, the target plate potential should be increased, since the net current from the target to the ground increases. The effective secondary electron emission coefficient is given by

$$\delta = (2.72)^2 \frac{\delta_m}{k_B T_e} \int_0^\infty \frac{\varepsilon}{E_{pm}} \exp\left[-\frac{\varepsilon}{k_B T_e} - 2\sqrt{\frac{\varepsilon}{E_{pm}}} \right] d\varepsilon, \qquad (3.2)$$

where δ_m is the maximum value of the coefficient, E_{pm} is primary electron energy with δ_m, and T_e is effective temperature of the primary electron [29]. Figure 3.2.4 shows effective coefficients for carbon (δ_m = 1, E_{pm} = 300 eV) and tungsten (δ_m = 1.35, E_{pm} = 650 eV). In the ICH period, inflow electrons to target plate consist of end loss electrons from core region. There is no difference between the effective coefficients of carbon and tungsten for the electron temperature in the core region (30-80 eV) as shown in Fig. 3.2.4. In the ECH period, inflow electrons consist of warm electrons heating by the ECH and cold electrons from core region. When the ground resistance is high (i.e. the target plate potential is negatively deep), effect of the warm electrons to secondary electron emission is dominant since inflow of the cold electrons to the target plate is prevented by sheath potential. For the warm electron temperature (550-750 eV) in the ECH period, the effective coefficient of tungsten is about 1.5 times higher than that of carbon, indicating that the secondary emission from the tungsten plate was much higher than that of carbon. On the other hand, when the resistance is low (i.e. the plate potential is nearly 0 V), most cold electrons inflow to the plate, and then, it is effective to secondary electron emission.

3.2.2. Effect of change in plate resistance

As shown in Fig. 3.2.2(b), the central plasma potential is increased by the ECH in every case of the carbon and tungsten plates and low and high ground resistances. There is no difference in the central plasma potential between the cases of the carbon and tungsten targets when the ground resistances were the same. The central plasma potential for the low resistance case (80 Ω) is higher than that for the high resistance case (280 kΩ). The potential decreased gradually with time. In the ECH period, the central plasma potential depends on the plug potential, which is produced by the enhanced electron loss due to the ECH at the plug region. When the plug potential increases, the central potential also increases, and vice versa. In fact, the plug potential was increased by the ECH and was gradually decreased in the ECH period as shown in Fig. 3.2.5. This gradual decrease in the plug potential causes the gradual decrease in the central plasma potential. The increase in the target plate potential shown in Fig. 3.2.2(a) was also caused by the decrease in the plug potential, since the number of the end loss ions which flowed to the target plate increased due to decrease in the plug potential.

When the resistance of the target plate is high, net current from the plate to ground is almost zero. Therefore, inflow of warm electron to the plate is restricted, that is, plug potential is low. On the other hand, when the resistance is low, inflow of warm electron to the plate is large and plug potential is high. The confinement potential prevents that ion in central region flow out toward end region. So, central potential increase when plug potential increase. This may be one of the reasons that central potential for the low resistance case is higher than that of the high resistance case. The potential in the ECH period deceased gradually. This seems to be attributed to decrease in the plug potential (i.e. confinement potential). It should be noticed that the core plasma potentials for the case of carbon and tungsten target plates with the ground resistance of 280 kΩ were the same, even though the flouting potentials of the both target plates were much different from each other.

3.2.3. Radial potential and electric field formation

Figure 3.2.6(a) and (b) shows the radial central potential in the ICH period and ECH period in the case of the plate resistance 280 kΩ. In the ICH period, potential profile in the projected region of the target plate was almost flat, and potential in the outer side of the projected region increased. When the ECH was injected, the central

potential increased about 60 V in the center region, and the radial potential profile was flat, and so there were no radial electric field. Figure 3.2.7(a) and (b) shows the radial central potential in the ICH period and ECH period in the case of the plate resistance 80 Ω. In the ICH period, potential profile in the projected region of the target plate was also almost flat, and potential in the outer side of the projected region increased. However, when the ECH was injected, the central potential increased about 200 V in the projected region, and potential profile was concave down. The increment of potential in the projected region of the target plate was significant. As previously explained, plug potential of the high resistance case is higher and central potential also increase. It is presume that plug potential was high significantly in the projected region of the target plate in the low resistance case (80 Ω). Therefore, Central potential in the projected region was also high significantly. Strong radial electric field formed outside the projected region by this increase of potential in the projected region. On the other hand, electric field in the projected region was weak. For example, electric fields with the insertion of carbon target were 2.8 V/cm (at about 0-4 cm), 12.7 V/cm (at about 4-9 cm) and 3.3 V/cm (at about 9-15 cm), respectively.

3.2.4. Generation of fluctuation

In the case of the resistance 80 Ω, characteristic fluctuation was observed. On the other hand, this fluctuation was not observed in the case of the resistance 280 kΩ (i.e. in the case of no radial electric field as shown in Fig. 3.2.6(b)). Figure 3.2.8 and 3.2.9 show the central potential and density fluctuation spectra at X ~ 0 cm with the insertion of carbon target and tungsten target which were grounded through the 280 kΩ, respectively. It is seen that characteristic fluctuation don't occur in the case of no radial electric field. On the other hand, characteristic fluctuation was observed at X ~ 0 cm in the case of the resistance 80 Ω as shown in Fig. 3.2.10. The characteristic fluctuation was also observed on the target potential fluctuation as shown in Fig. 3.2.11 and on the line density fluctuation as shown in Fig. 3.2.12. The characteristic fluctuation was observed at about 13 kHz. The frequency of the fluctuation on the target plate is equal to it of the central plasma fluctuations. It is indicated that the target plate potential is correlated to the central plasma. Figure 3.2.13 and 3.2.14 show the radial distribution of central potential and density fluctuation spectra with the insertion of carbon target and tungsten which was grounded through the 80 Ω resistances, respectively. This fluctuation in this experiment has unique features. The potential fluctuation level was strongest at about 4-9 cm, and this position almost agreed with the position in where electric field was strongest (about 4-9 cm). On the other hand, the density fluctuation level was very weak in the region of large electric field and strong in the projected region of the plate. Then, the potential and density fluctuations disappear in the peripheral region. The fluctuation which has unique and new feature is observed in this experiment.

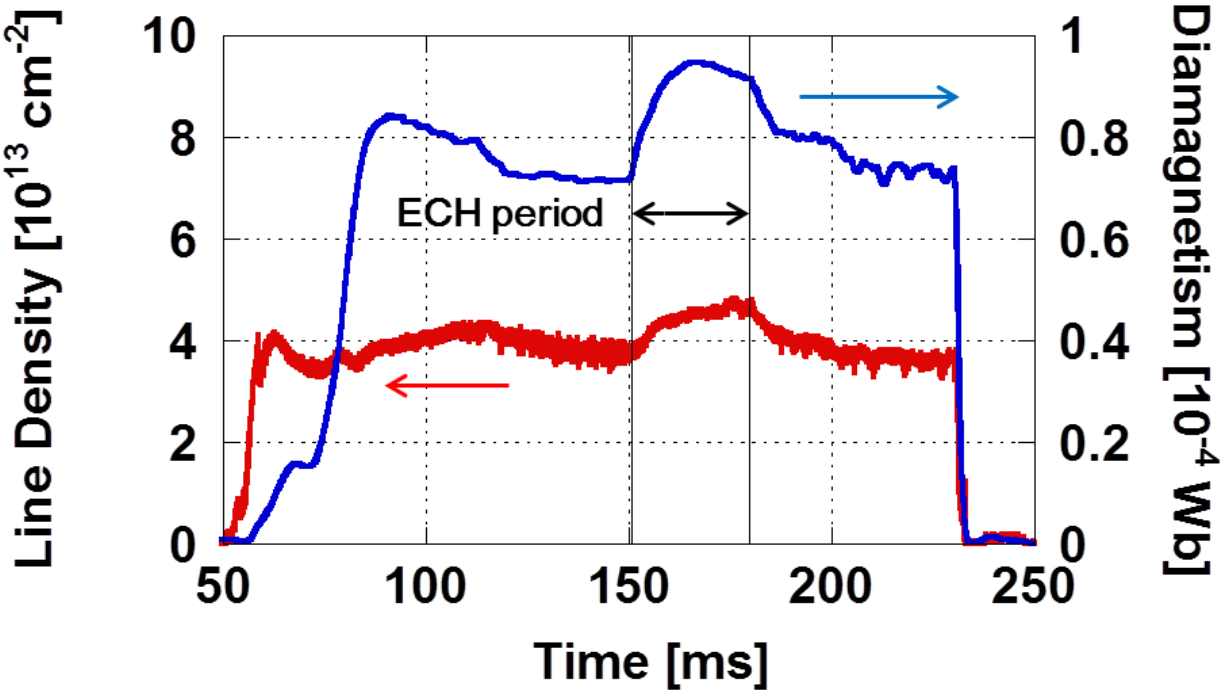

Fig. 3.1.1. The time evolution of the line density and the diamagnetism of the central plasma. The plug ECH is applied from 151 ms to 180 ms.

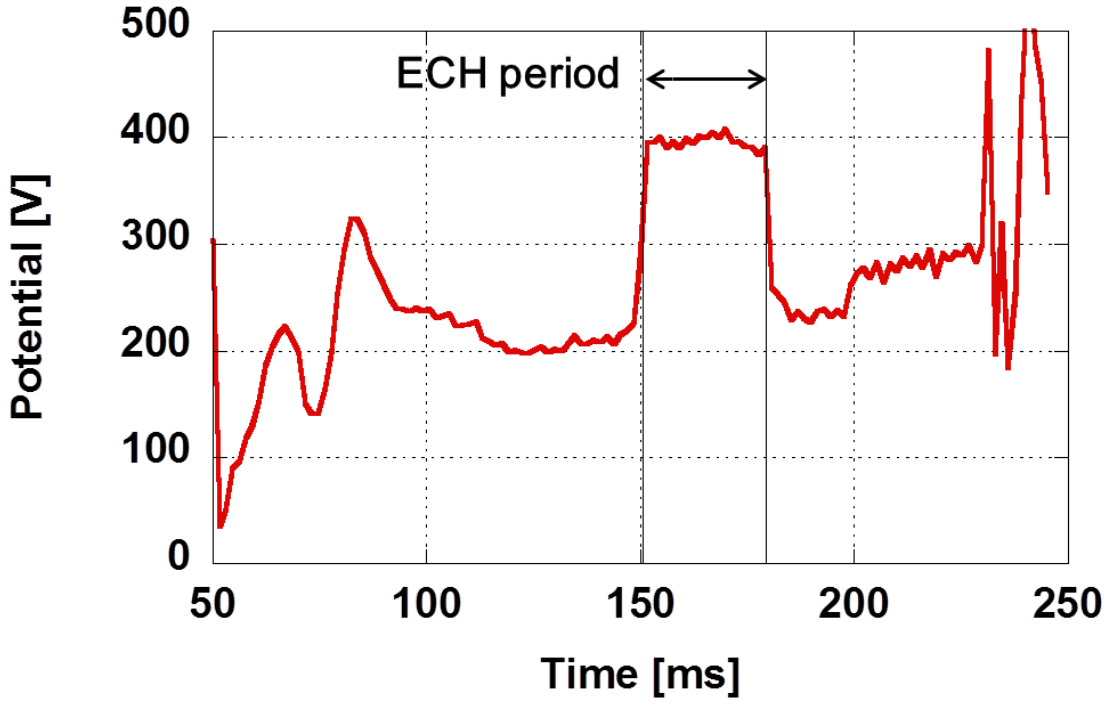

Fig. 3.1.2. The time evolution of the potential of the central plasma.

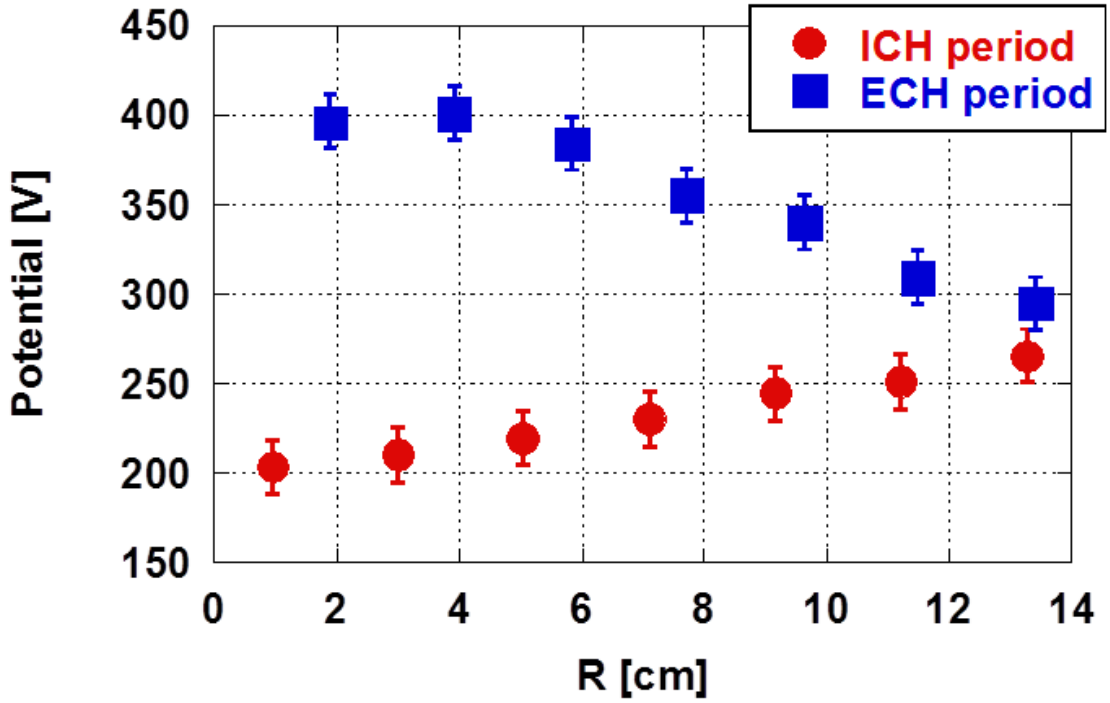

Fig. 3.1.3. The radial profile of the potential during the ICH period and the ECH period.

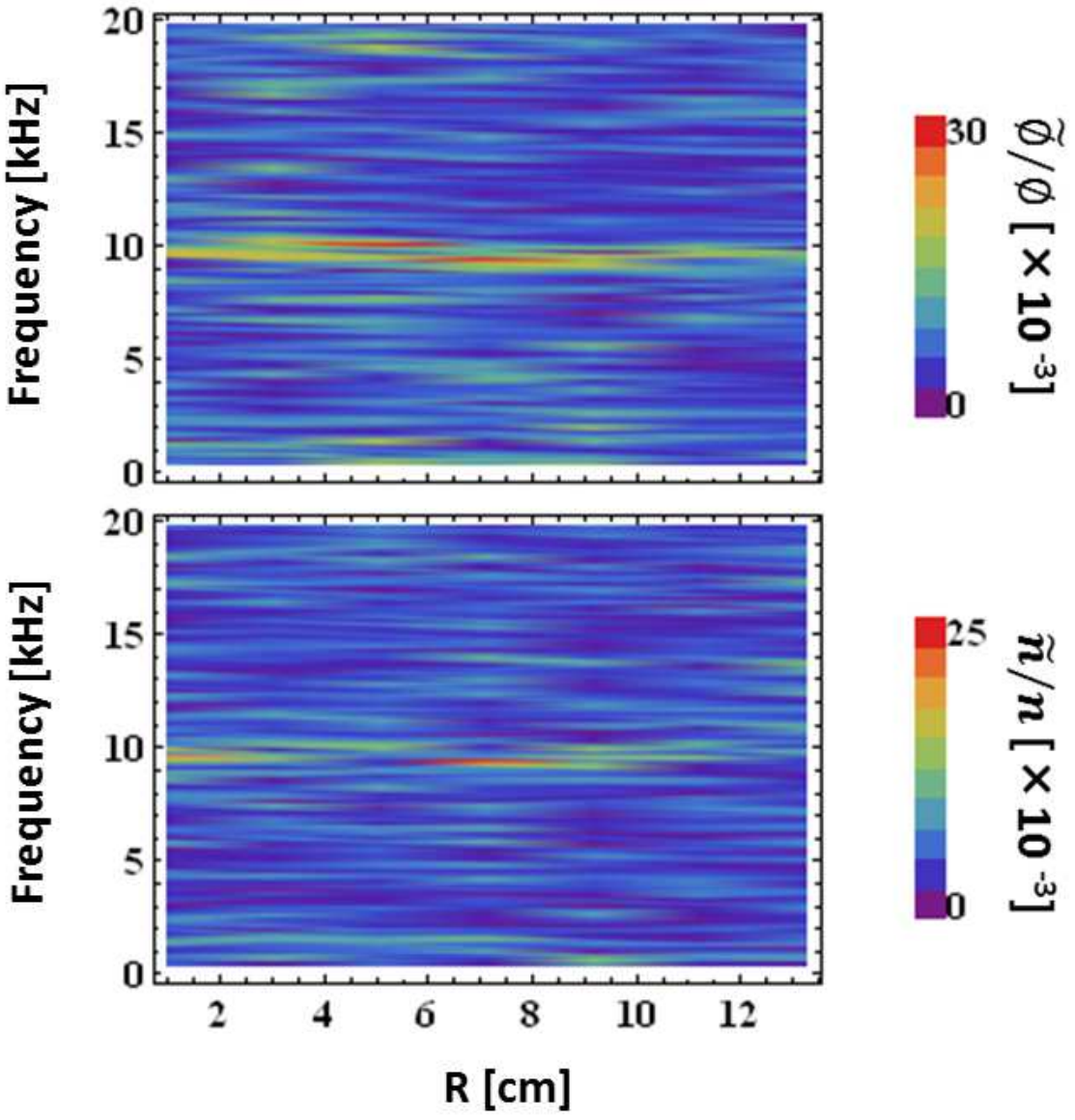

Fig. 3.1.4. The radial profile of the potential and density fluctuation spectra during the ICH period.

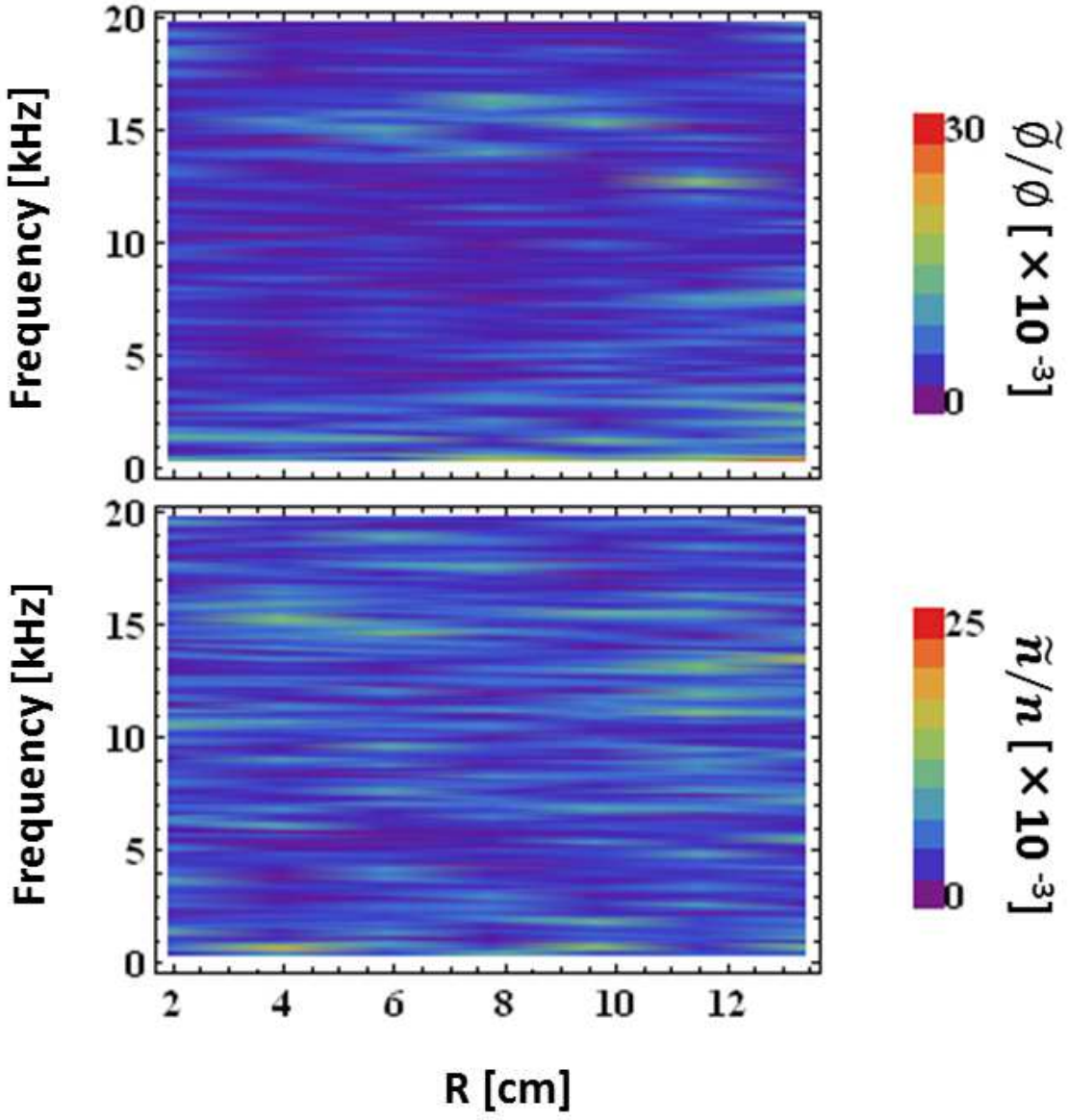

Fig. 3.1.5. The radial profile of the potential and density fluctuation spectra during the ECH period.

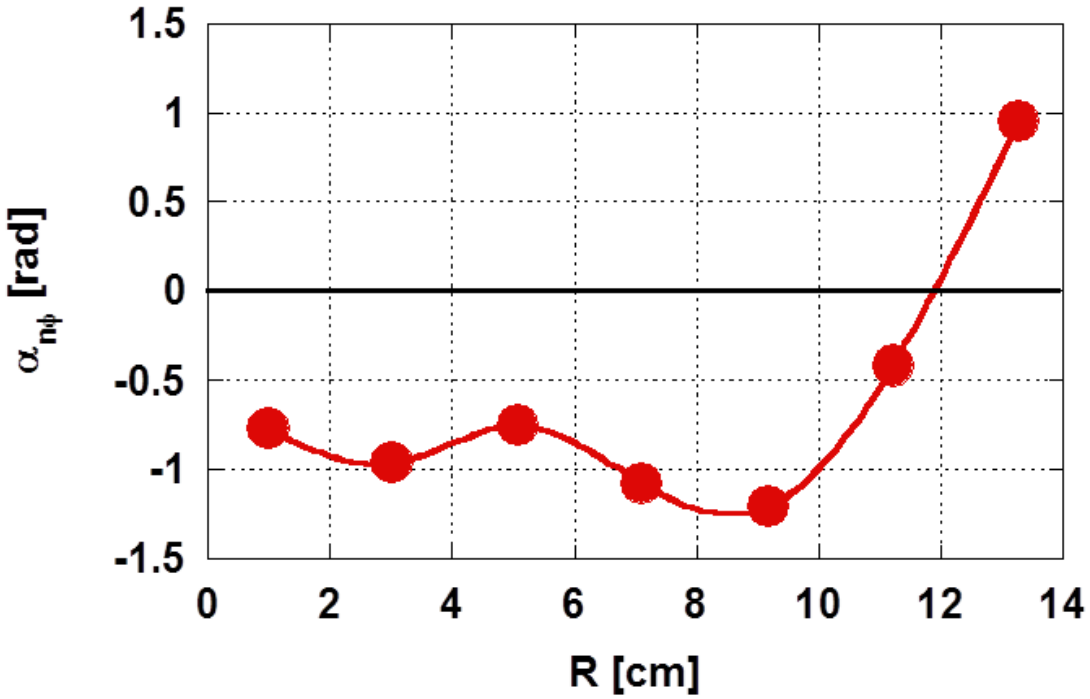

Fig. 3.1.6. The radial profile of the difference phase between potential and density fluctuation $\alpha_{n\varphi}$ during the ICH period.

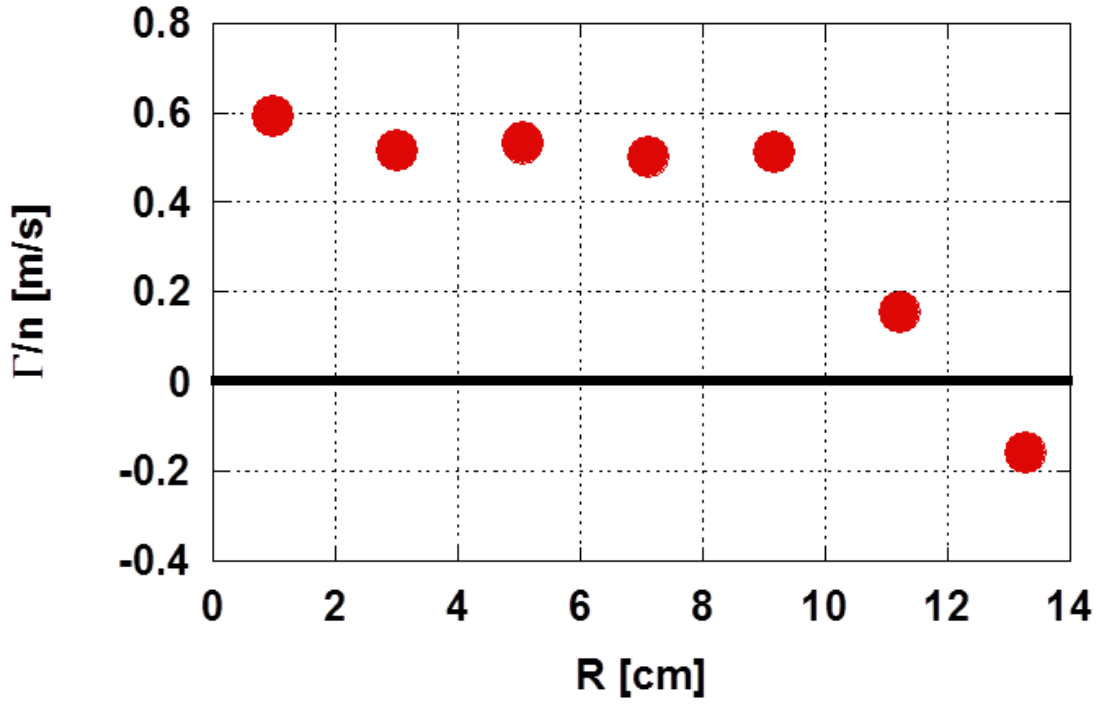

Fig. 3.1.7. The radial profile of normalized particle flux in the ICH period. The particle flux was calculated from the difference phase between potential and density fluctuation.

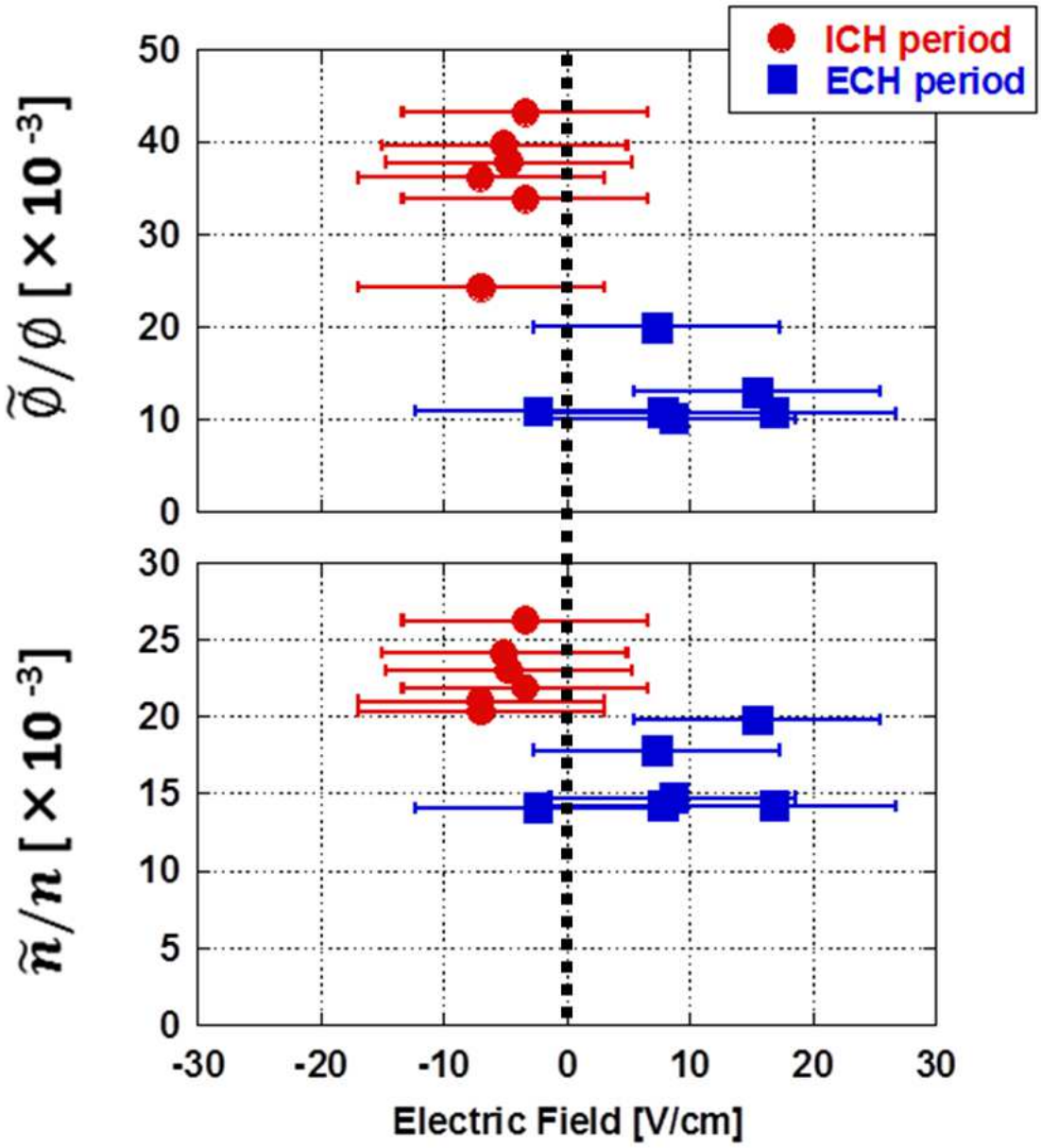

Fig. 3.1.8. The relationship between the electric field strength and the fluctuation level during the ICH period and ECH period.

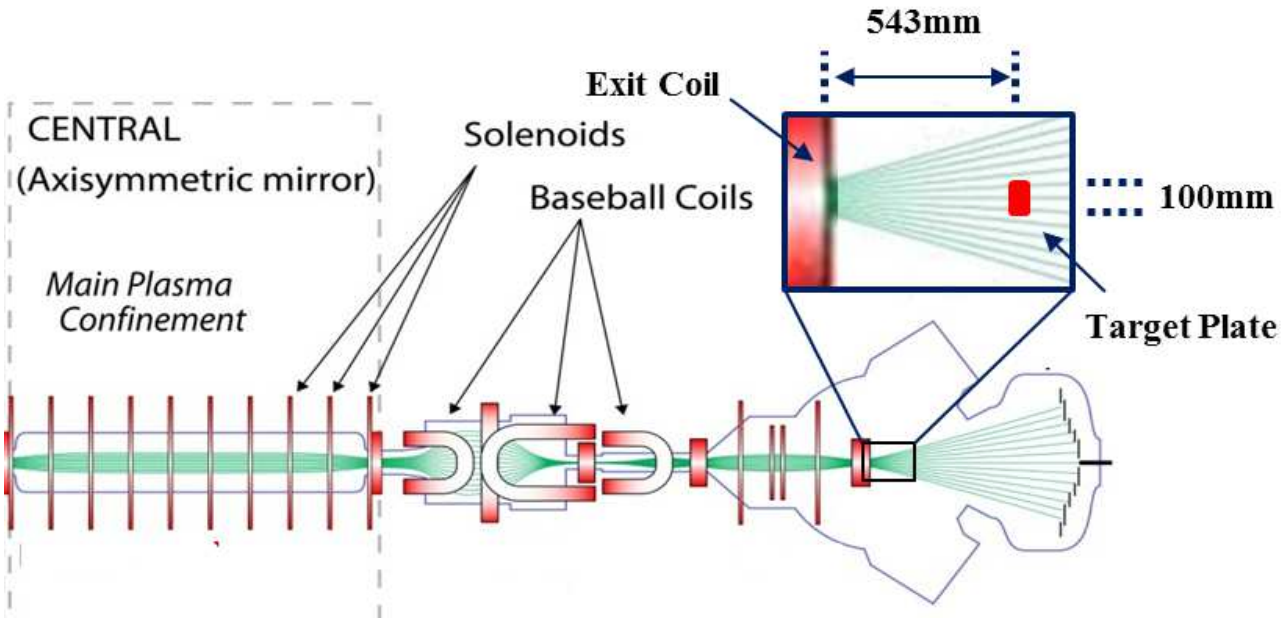

Fig. 3.2.1. The schematic view of the target plate. The target plate was inserted to the west end region. The diameter of plate is 100 mm. And the plate was inserted at 543 mm from the exit of the west end coil (i.e. at Z = 10.74 m).

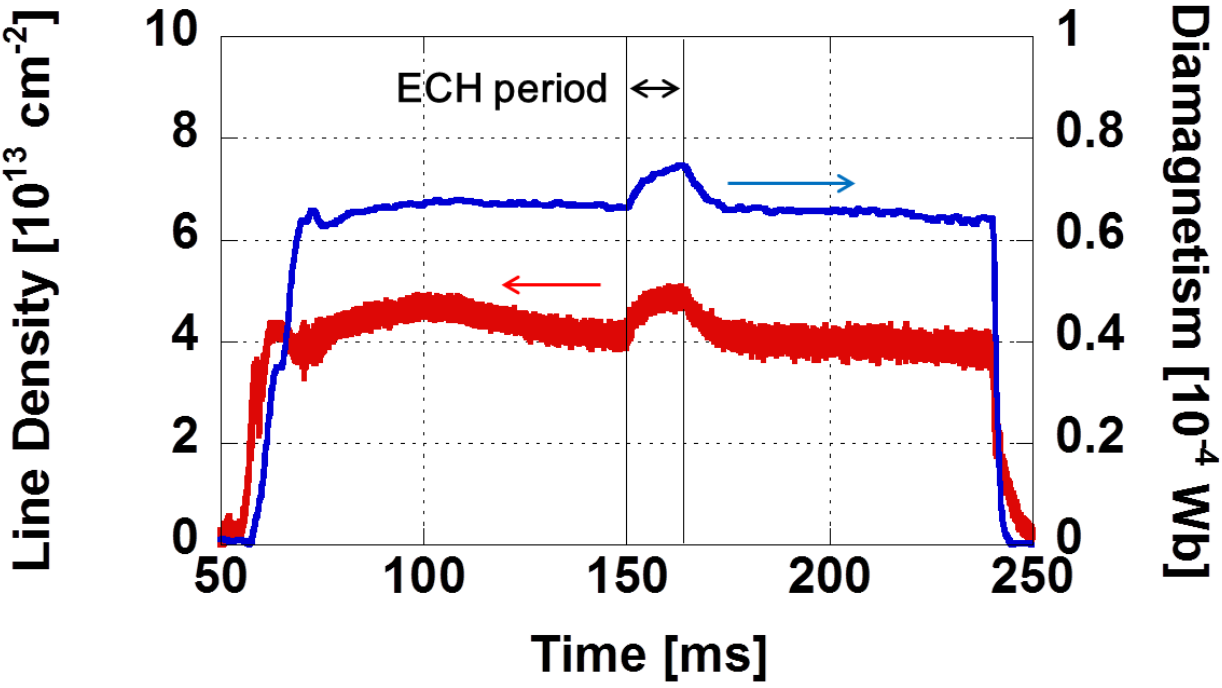

Fig. 3.2.2. The time evolution of the line density and the diamagnetism of the central plasma. The plug ECH is applied from 150 ms to 165 ms.

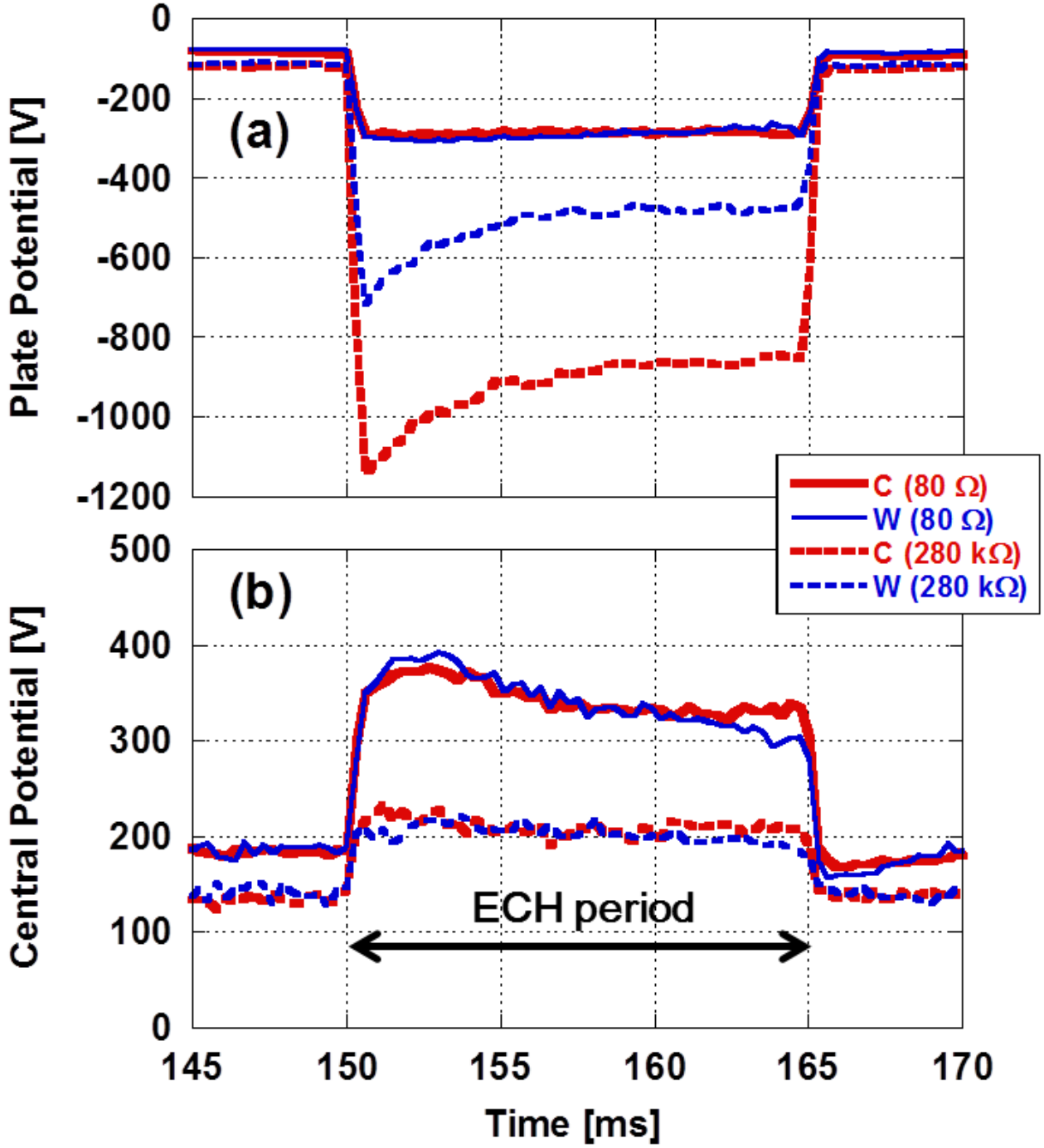

Fig. 3.2.3. The time evolution of (a) the potential of the target plate of carbon and tungsten and (b) the central plasma potential in the cases of the ground resistance of 80 Ω and 280 kΩ.

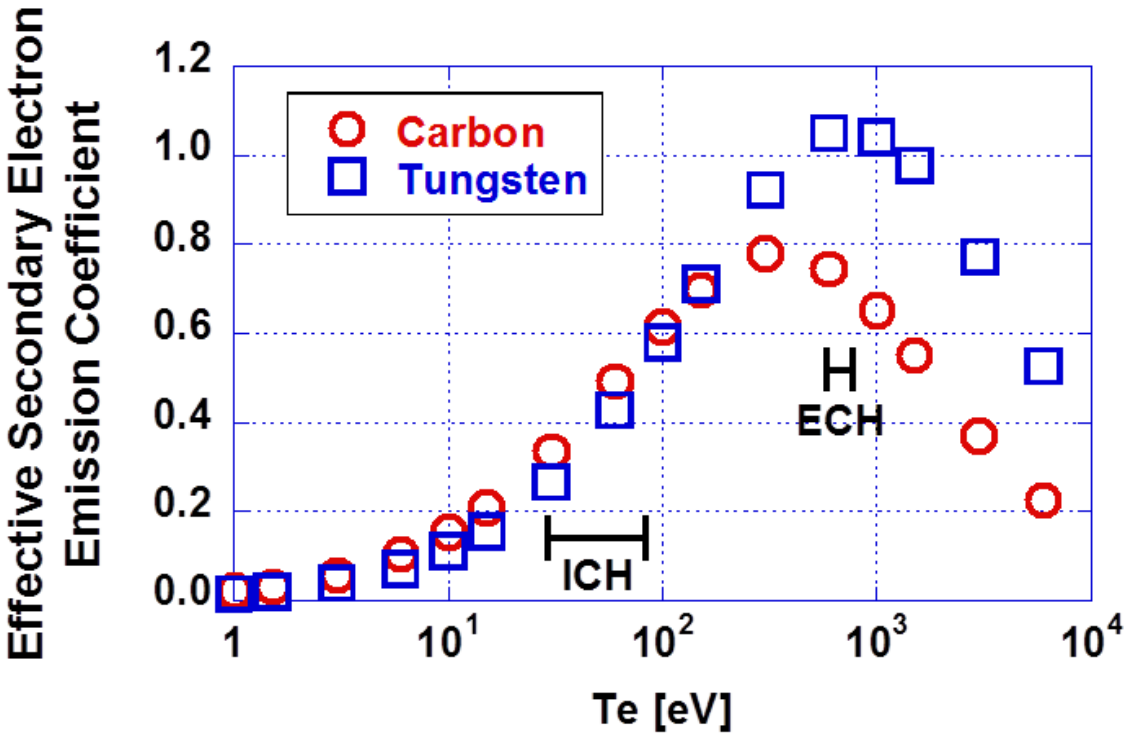

Fig. 3.2.4. Effective secondary electron emission coefficients for carbon and tungsten as a function of the electron temperature.

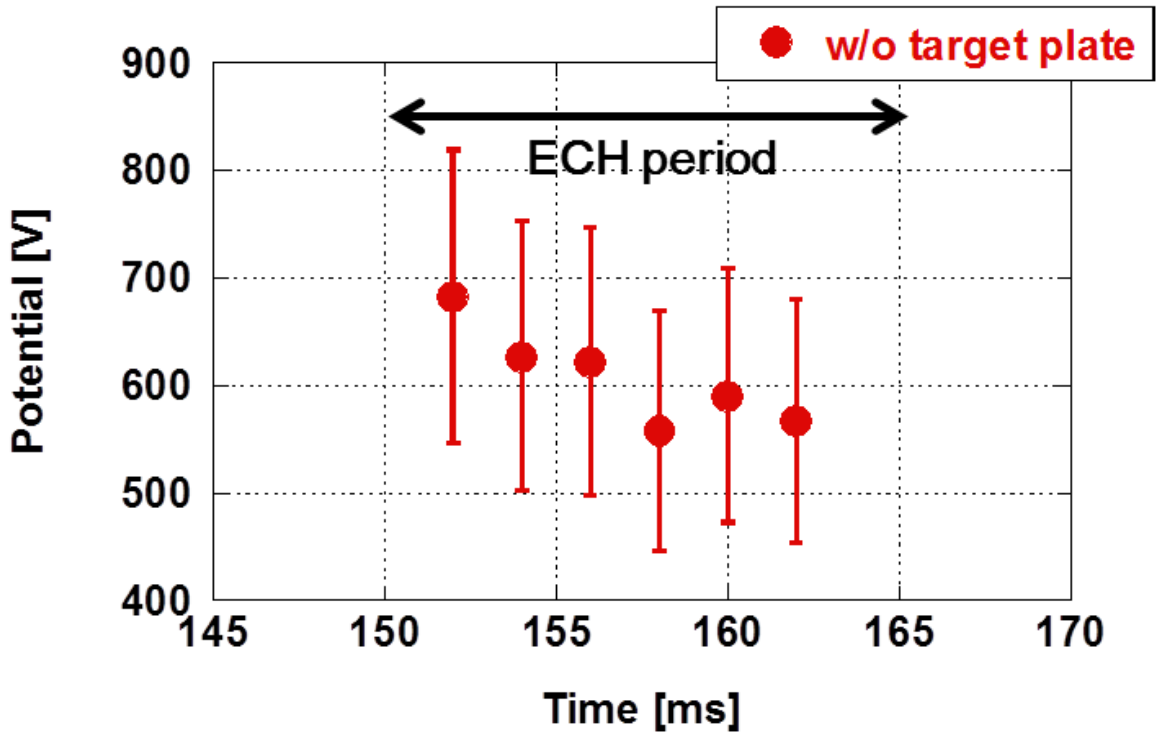

Fig. 3.2.5. The time evolution of the plug potential which was measured by the ELIEA. The data was obtained without the target plate in the same experimental condition except the target plate, since the target plate was on the same magnetic field line as the ELIEA.

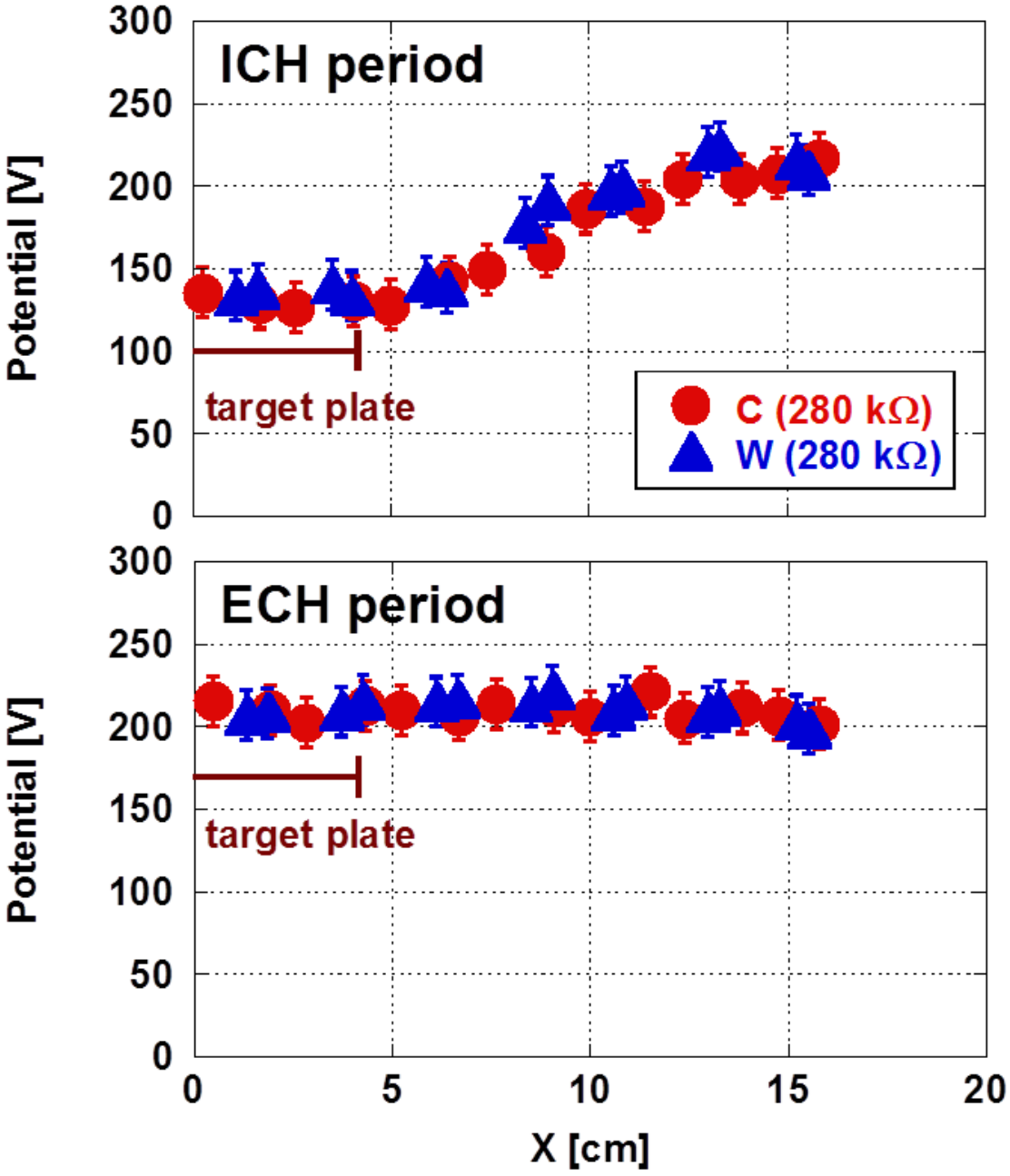

Fig. 3.2.6. The spatial distribution of the central potential during (a) the ICH period and (b) ECH period in the case of the ground resistance of 280 kΩ. The bar indicates the target plate area projected to the central region.

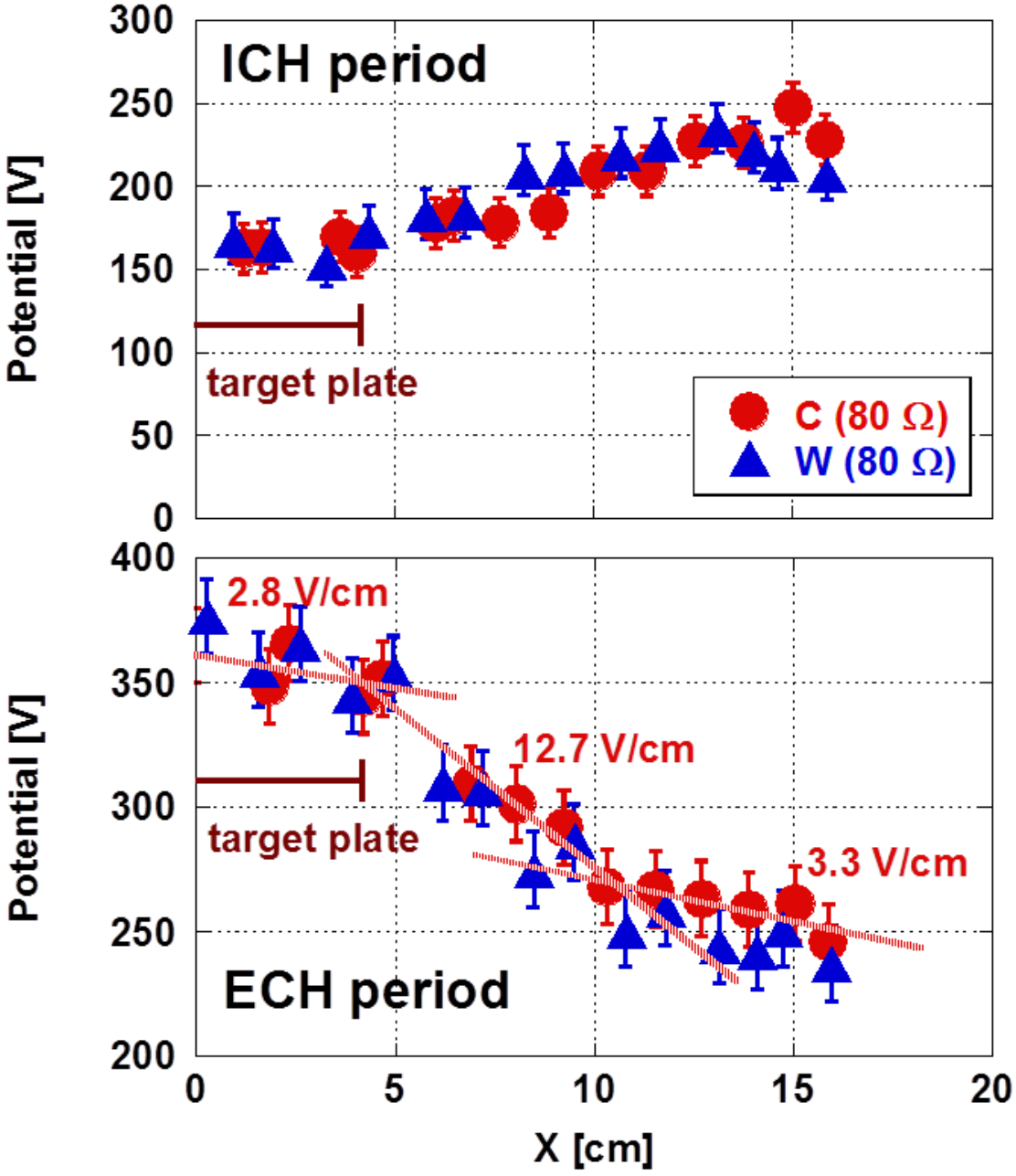

Fig. 3.2.7. The radial central potential during ICH period (a) and ECH (b) period in the case of the plate resistance 80 Ω

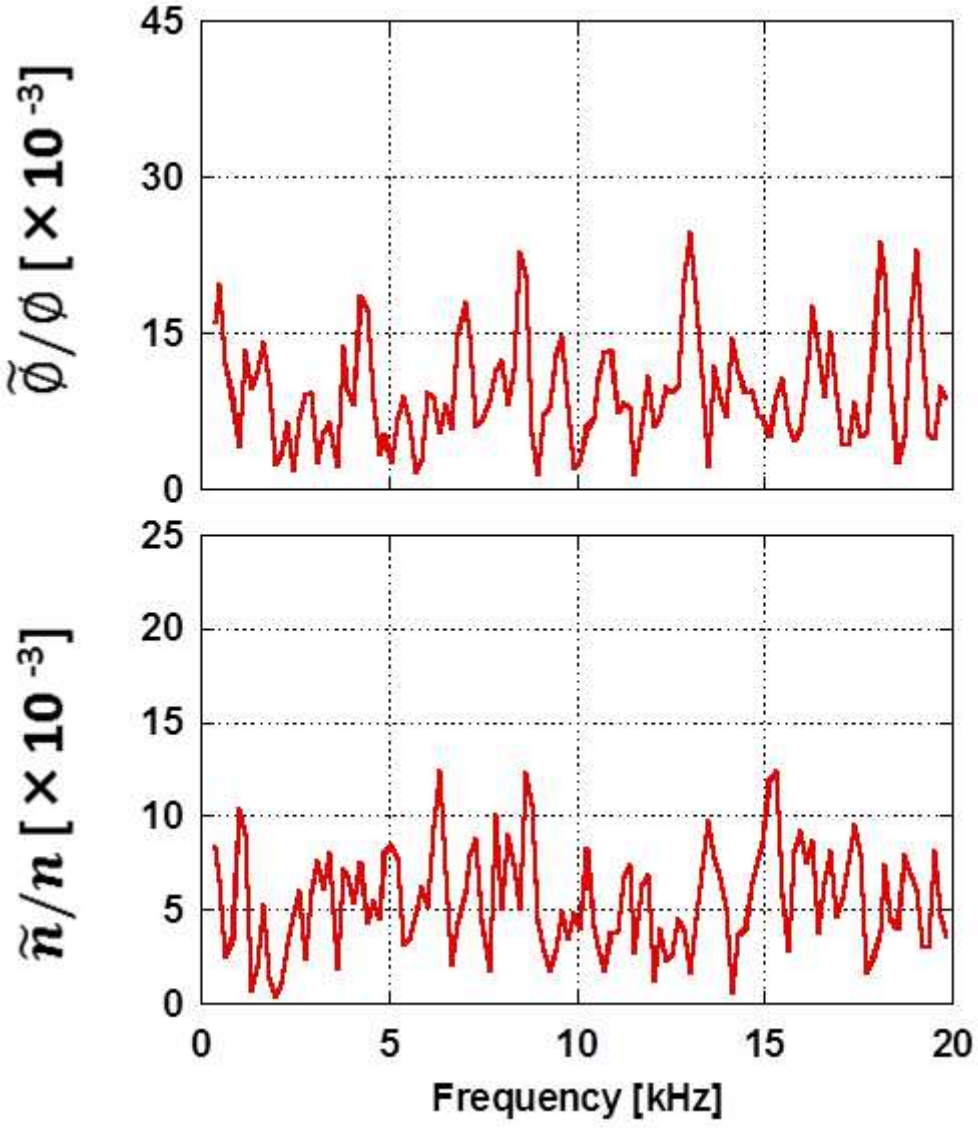

Fig. 3.2.8. The central potential fluctuation spectra and density fluctuation spectra at X ~ 0 cm with the insertion of carbon target which was grounded through the 280 kΩ resistances.

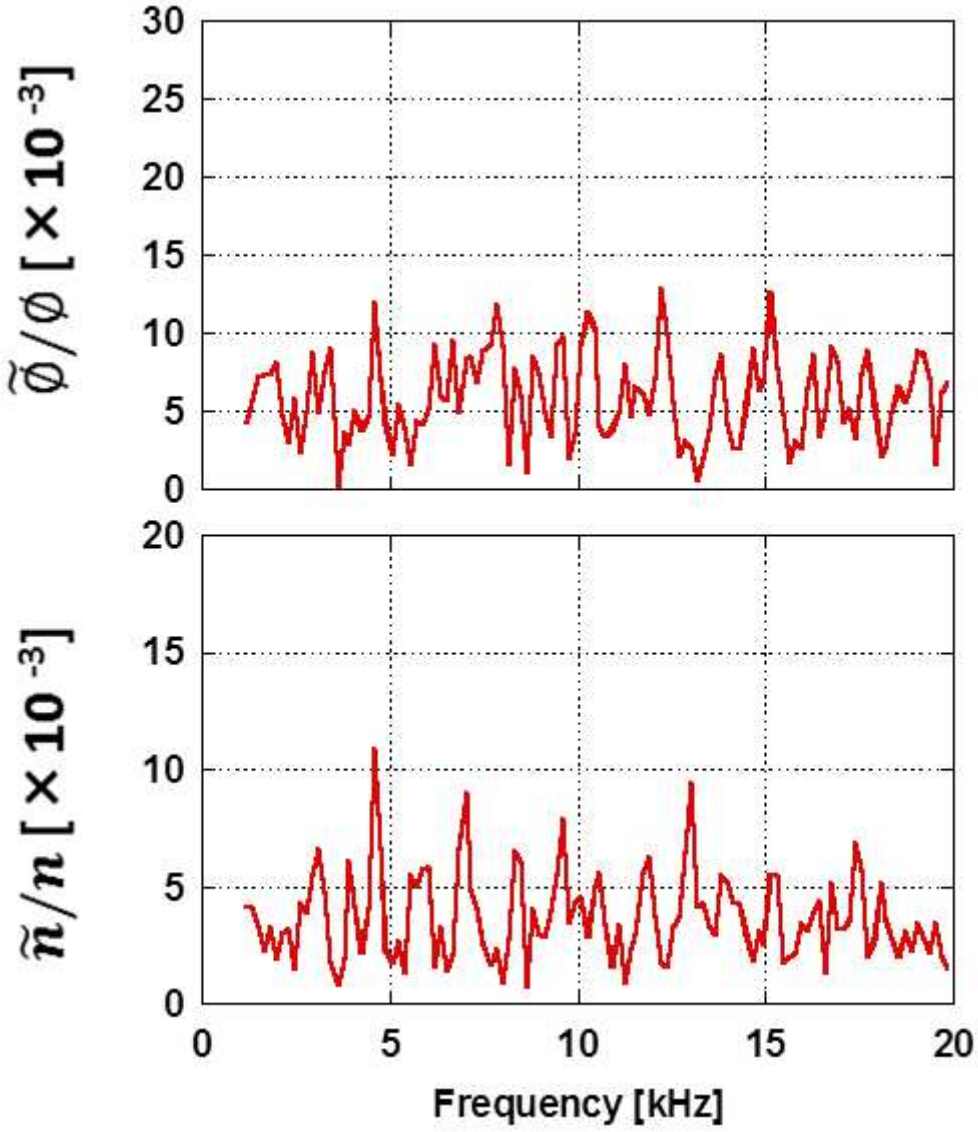

Fig. 3.2.9. The central potential fluctuation spectra and density fluctuation spectra at X ~ 0 cm with the insertion of tungsten target which was grounded through the 280 kΩ resistances.

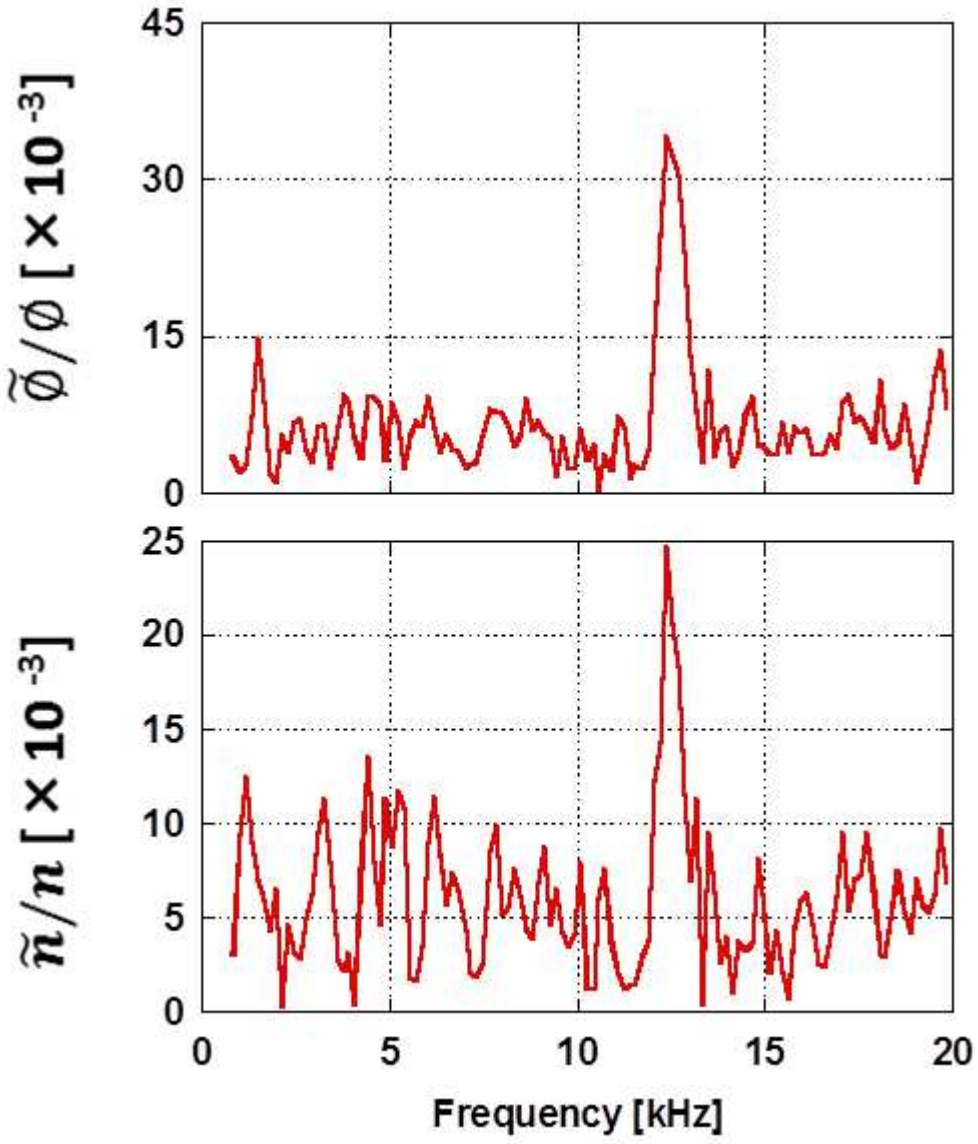

Fig. 3.2.10. The central potential fluctuation spectra and density fluctuation spectra at X ~ 0 cm with the insertion of carbon target which was grounded through the 80 Ω resistances.

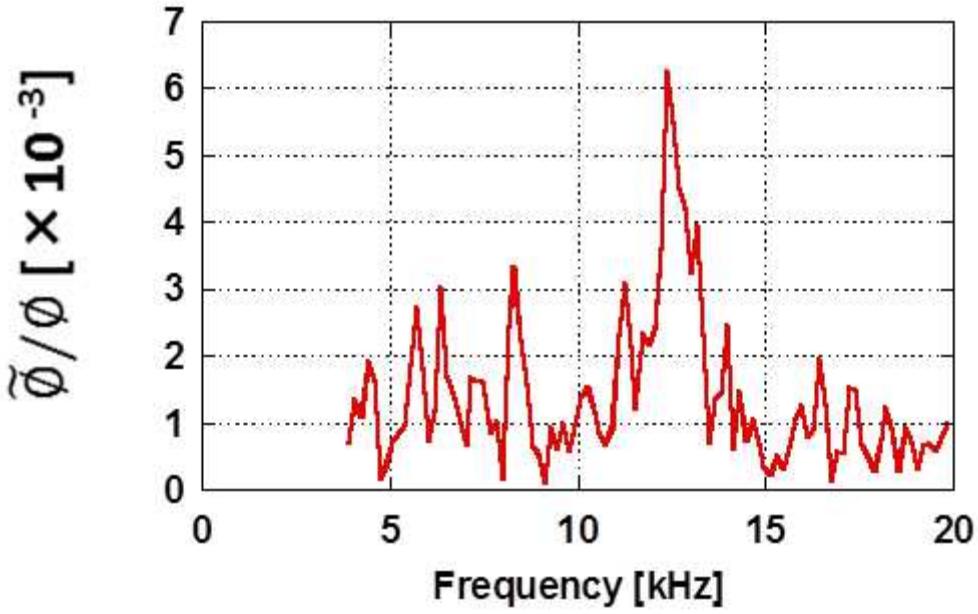

Fig. 3.2.11. The carbon target plate potential fluctuation spectra in the case of the resistance 80 Ω.

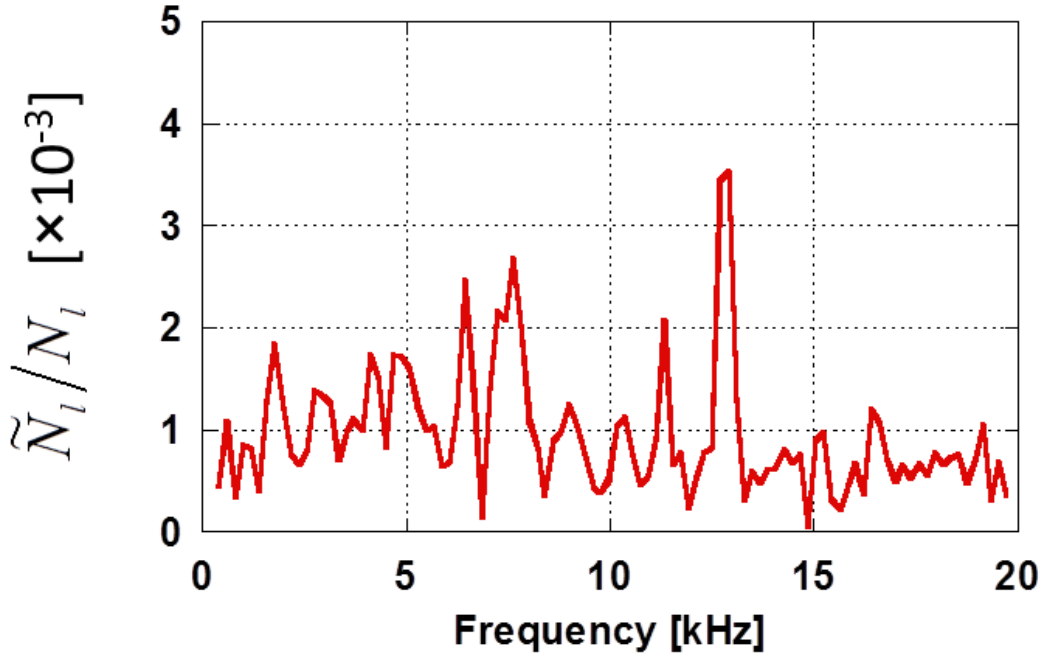

Fig. 3.2.12. The line density spectra measured by microwave interferometer at Y = 0 cm in the case of the carbon target plate insertion with resistance 80 Ω.

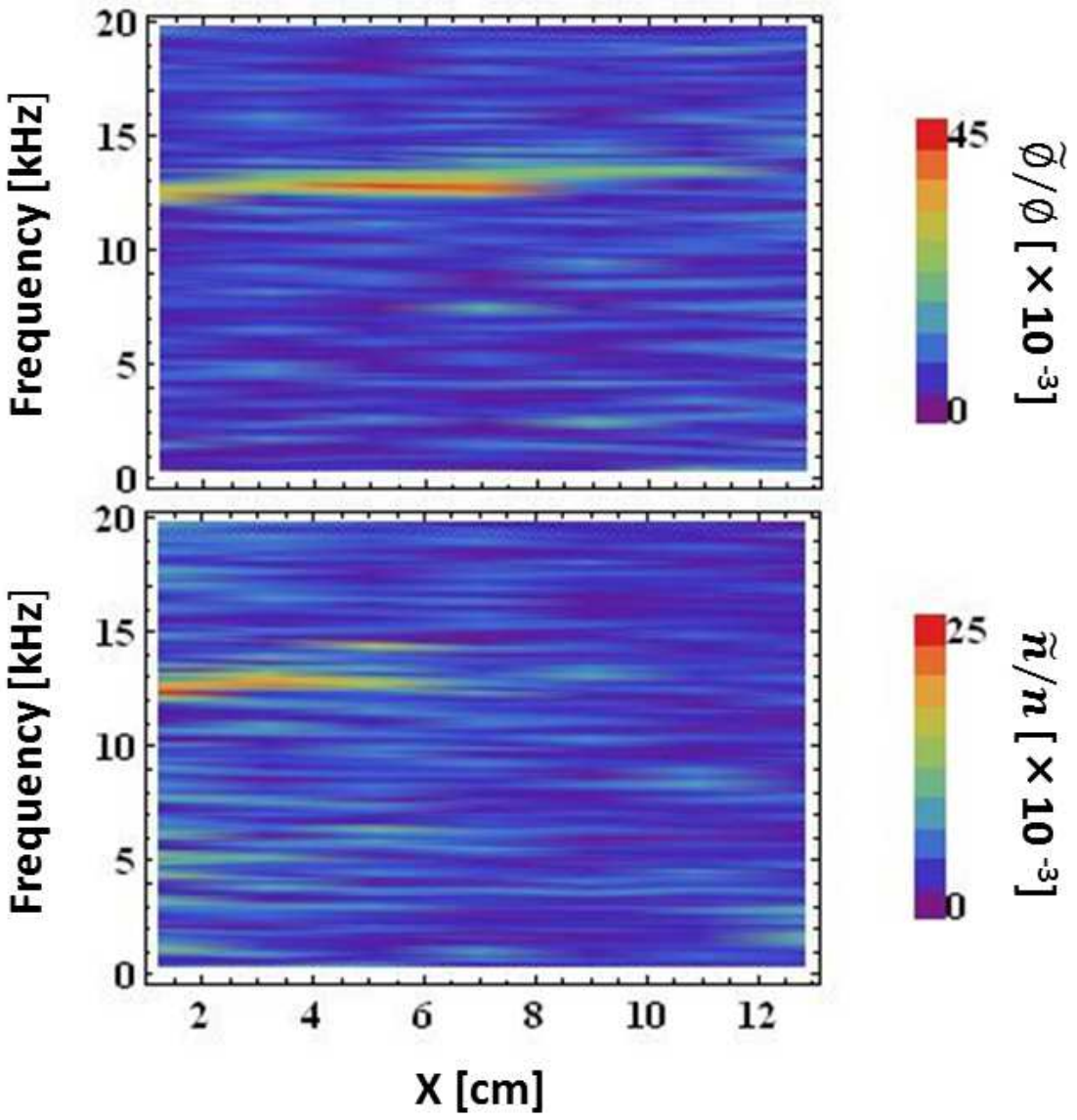

Fig. 3.2.13. The radial distribution of central potential fluctuation spectra and density fluctuation spectra with the insertion of carbon target which was grounded through the 80 Ω resistances. The fluctuation level rises as graph color approach red.

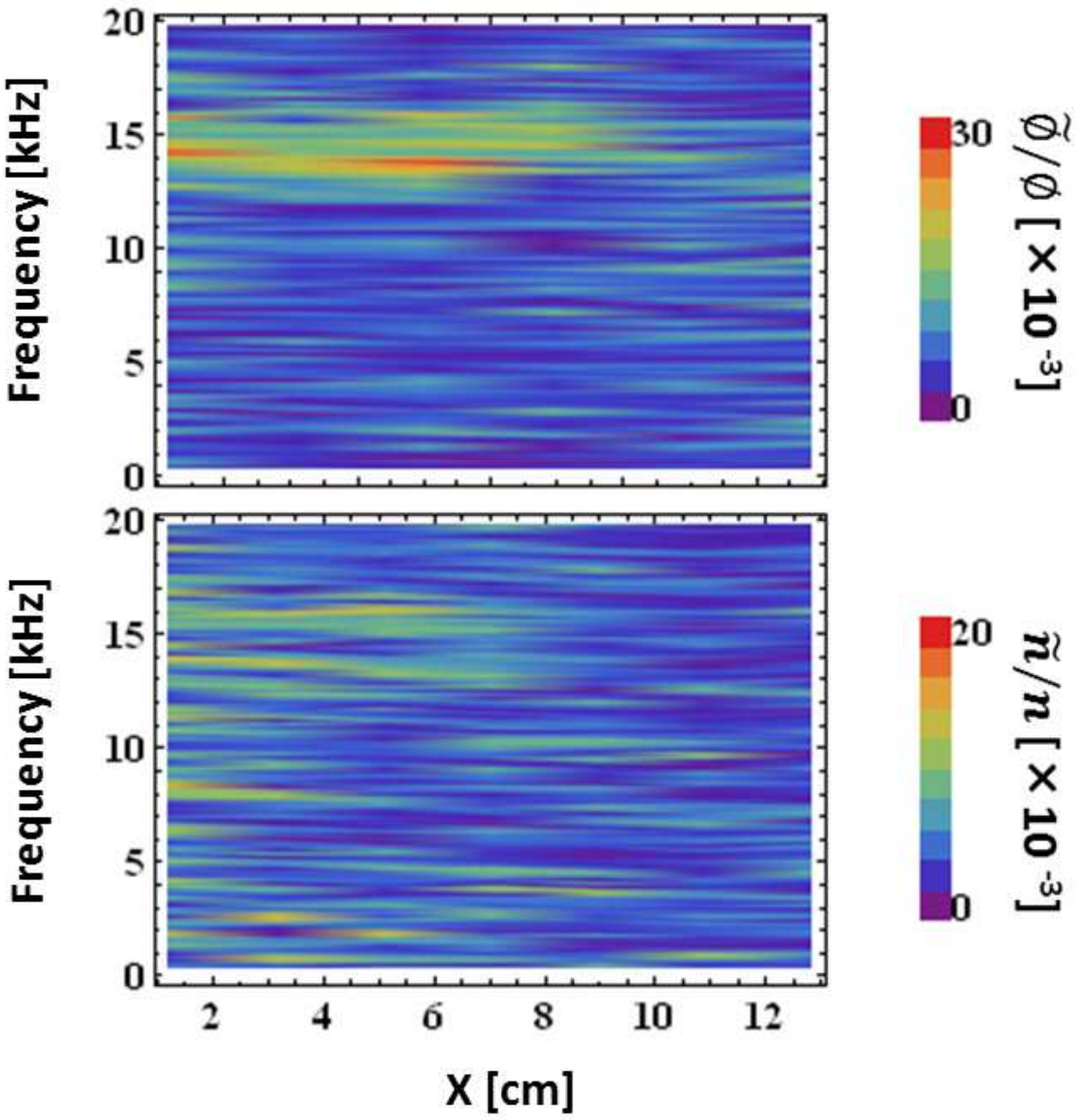

Fig. 3.2.14. The radial distribution of central potential fluctuation spectra and density fluctuation spectra with the insertion of tungsten target which was grounded through the 80 Ω resistances.

4. Summary

One of the most important issues in the magnetic confinement plasma is to study the relation between the electric field and the fluctuation. To study the relation between the electric field and the fluctuation, potential control methods (such as plasma heating, plasma biasing) was employed in various devices. In this thesis, the relation between the potential formation and the low frequency fluctuations was studied by using the following two kinds of methods for the potential formation control in GAMMA10 tandem mirror: (1) confinement potential formation by applying ECH and (2) the insertion of the target plate in the end region. Plasma potential, potential fluctuation, and density fluctuation was measured by a gold neutral beam probe (GNBP). The radial profile of the potential and fluctuations were measured shot by shot.

Firstly, the fluctuation suppression by applying the plug ECH and relation between radial electric field and fluctuation level have been studied. The drift type fluctuation was observed at about 10 kHz in the ICH period and the fluctuation was suppressed by applying the plug ECH. The radial profile of central potential was concave up and the radial electric field was negative in the ICH period. On the other hand, the radial profile of central potential was concave down and the radial electric field was positive in the ECH period. The E×B drift driven by positive electric field rotated in the opposite direction of the diamagnetic drift in the ECH period. It was observed that the electric field shear was weak in R = 0-14 cm. So, strong electric field shear which is effective to suppress the drift type fluctuation may exist in R = 14-20 cm.

Secondly, the target plate made of carbon or tungsten was inserted into the end region and changed the ground resistances to modify the potential profile. The central potential for the low resistance case (80 Ω) is very higher than that of the high resistance case (280 kΩ) in the ECH period. The increment of central potential in the projected region of the target plate was significant. When the ground resistance is low (80 Ω), strong radial electric field formed outside the projected region in the ECH period. On the other hand, electric field in the projected region was weak. The radial electric fields were 2.8 V/cm (at about 0-4 cm), 12.7 V/cm (at about 4-9 cm) and 3.3 V/cm (at about 9-15 cm), respectively.

In the case of the ground resistance of 80 Ω, the characteristic fluctuation was observed on the potential fluctuation and the density fluctuation in the ECH period. This fluctuation has the following unique features: (1) The potential fluctuation level was strong in the region of large electric field. (2) The density fluctuation level was very weak in the region of large electric field and strong in the projected region of the plate. (3) The potential and density fluctuations disappear in the peripheral region. The characteristic fluctuation which has these interesting features was discovered by the insertion of the low resistance target plate.

Acknowledgments

The author would like to express his sincere gratitude to Professor M. Sakamoto for his helpful discussions and suggestions in the course of the present study.

The author especially thanks to Professor M. Yoshikawa, Professor Y. Nakashima, and Professor T. Imai for their helpful discussions and significant suggestions.

The author would like to thank members of the Beam Probe group for their collaboration earnestly.

Finally, the author would like to thank all member of the GAMMA10 group for carrying out the interesting experiments and helpful suggestions.

References

[1] A.H. Bekheit; J. Fusion Energ. **27**, 338–345 (2008)

[2] K.H. Burrell; Phys. Plasmas. **4** (1997) 1499-1518

[3] T. S. Hahm, K. H. Burrell; Phys. Plasmas. **3** (1996) 427-429

[4] P. H. Diamond, Y. M. Liang, et al; Phys. Rev. Let. **72** (1994) 2565-2568

[5] A. S. Ware, P. W. Terry, et al; Plasma Phys. Cont. Fusion. **38** (1996) 1343-1347

[6] B. A. Carreras, K. Sidikman, et al; Phys. Fluids B. **4** (1992) 3115-3131

[7] K. L. Sidikman, B. A. Carreras, et al; Phys. Plasmas **1** (1994) 1142-1153

[8] R. A. Moyer, K. H. Burrell, et al; Phys. Plasmas. **2** (1995) 2397-2407

[9] A. S. Ware, P. W. Terry, et al; Phys. Plasmas. **5** (1998) 173-177

[10] P. W. Terry, D. E. Newman, A. S. Ware; Phys. Rev. Let. 87 (2001)

[11] M. Yoshikawa, Y. Miyata, et al; Fusion Sci. Tec. **59** (2011) 232-234

[12] M. Mizuguchi, M. Yoshikawa, et al; Fusion Sci. Tec. **55** (2009) 82-86

[13] J. L. Velasco, F. Castejon; Plasma Phys. Cont. Fusion. **54**(2012)

[14] T. S. Hahm, D. H. Na, et al; Nuclear Fusion. **53** (2013)

[15] A. Kojima, K. Ishii, et al; J. of Korean Phys. Society. **49** (2006) 100-104

[16] A. Kojima. Doctoral Program in Physics at the University of Tsukuba

[17] S. J. Zweben, M. D. Campanell, et al; Plasma Phys. Cont. Fusion **54** (2012) 1-16

[18] J. Stockel, P. Devynck, et al; Plasma Phys. Cont. Fusion. **47** (2005) 635-643

[19] S. Kitajima, H. Takahashi, et al; Nucl. Fusion. **51** (2011) 1-5

[20] G. F. Counsell, J. W. Ahn, et al; J. of Nucl. Materials **313-316** (2003) 804-812

[21] T. Tokuzawa, A. Mase, et al; Jpn. J. Appl. Phys. **33** (1994) 807-809

[22] A. Mase, A. Itakura, et al; Nucl. Fusion **31** (1991) 1725-1733

[23] K. Ishii, A. Miyata, et al; Cze. J. of Phys. **55** (2005) 285-294

[24] R. Hatakeyama, T. Kaneko; Phys. Scripta. **T107** (2004) 200-203

[25] S. Tanaka, M. Ichimura, et al; Rev. of Sci. Instru. **70** (1999) 979-982

[26] Y. Tatematsu, T. Saito, et al; J. Plasma Fusion Res. Series **4** (2001) 387-390

[27] S. Takamura, M. Y. Ye, et al; Phys. Plasmas **5** (1998) 2151-2158

[28] K. Shiraishi, N. Ohno, et al; J. Nucl. Materials **196-198** (1992) 745-749

[29] T. Tawaraya, A. Tsushima, and S. Yoshimura; Japan. J. Applied Phys. **51** (2012)